Temporal variability of lagoon–sea water exchange and seawater circulation through a Mediterranean barrier beach

Joseph Tamborski, Pieter Van Beek, Valenti Rodellas, Christophe Monnin, Erwin Bergsma, Pierre Anschutz, Thomas Stieglitz, Christina Heilbrun, J. Kirk Cochran, Celine Charbonnier, et al.

Temporal variability of lagoon-sea water exchange and seawater circulation through a Mediterranean barrier beach

Joseph Tamborski[1], Pieter van Beek[1], Valentí Rodellas[2], Christophe Monnin[3], Erwin Bergsma[1], Thomas Stieglitz[2,4], Christina Heilbrun[5], J. Kirk Cochran[5], Céline Charbonnier[6], Pierre Anschutz[6], Simon Bejannin[1], Aaron Beck[7]*

Running Head: lagoon-sea exchange & circulation fluxes

Keywords: lagoons; circulation; submarine groundwater discharge; radium; radon; GEOTRACES

[1]LEGOS, Laboratoire d'Etudes en Géophysique et Océanographie Spatiales (Université de Toulouse, CNES, CNRS, IRD, UPS), Observatoire Midi Pyrénées, 14 Ave Edouard Belin, 31400 Toulouse, France

[2]Aix-Marseille Université, CNRS, IRD, INRA, Coll France, CEREGE, Europôle de l'Arbois, BP80, 13545 Aix-en-Provence, France

[3]GET, Géosciences Environnement Toulouse (Université de Toulouse, CNRS, IRD, UPS), Observatoire Midi Pyrénées, 14 Ave Edouard Belin, 31400 Toulouse, France

[4]Centre for Tropical Water & Aquatic Ecosystem Research, James Cook University, Townsville QLD 4811, Australia

[5]School of Marine & Atmospheric Sciences, Stony Brook University, Stony Brook, NY 11794 USA

[6]EPOC, Environnements et Paléoenvironnements Océaniques et Continentaux, Université de Bordeaux, CNRS, UMR 5805, Talence, France

[7]GEOMAR Helmholtz Centre for Ocean Research Kiel, Wischhofstr. 1-3, 24148, Kiel, Germany

*Corresponding author: jtamborski@whoi.edu

*Current address: Department of Marine Chemistry and Geochemistry, Woods Hole Oceanographic Institution, Woods Hole, MA 02536, USA

Co-author emails:
pieter.van-beek@legos.obs-mip.fr; rodellas@cerege.fr; christophe.monnin@get.omp.eu; erwin.bergsma@legos.obs-mip.fr; stieglitz@cerege.fr; christina.heilbrun@stonybrook.edu;

kirk.cochran@stonybrook.edu; celine.charbonnier@u-bordeaux.fr; pierre.anschutz@u-bordeaux.fr; simon.bejannin@legos.obs-mip.fr, ajbeck@geomar.de

ABSTRACT

The subterranean flow of water through sand barriers between coastal lagoons and the sea, driven by a positive hydraulic gradient, is a net new pathway for solute transfer to the sea. On the sea-side of sand barriers, seawater circulation in the swash-zone generates a flux of recycled and new solutes. The significance and temporal variability of these vectors to the French Mediterranean Sea is unknown, despite lagoons constituting ~50% of the coastline. A one-dimensional $^{224}Ra_{ex}/^{223}Ra$ reactive-transport model was used to quantify water flow between a coastal lagoon (La Palme) and the sea over a six-month period. Horizontal flow between the lagoon and sea decreased from ~85 cm d^{-1} during May 2017 (0.3 m^3 d^{-1} m^{-1} of shoreline) to ~20 cm d^{-1} in July and was negligible in the summer months thereafter due to a decreasing hydraulic gradient. Seawater circulation in the swash-zone varied from 10 – 52 cm d^{-1} (0.4 – 2.1 m^3 d^{-1} m^{-1}), driven by short-term changes in the prevailing wind and wave regimes. Both flow paths supply minor DSi fluxes on the order of ~3 – 10 mmol Si d^{-1} m^{-1}. Lagoon-sea water exchange supplies a net DIC flux (320 – 1,100 mmol C d^{-1} m^{-1}) two orders of magnitude greater than seawater circulation and may impact coastal ocean acidification. The subterranean flow of water through sand barriers represents a significant source of new DIC, and potentially other solutes, to the Mediterranean Sea during high lagoon water-level periods and should be considered in seasonal element budgets.

INTRODUCTION

Subterranean water exchange between coastal lagoons and the coastal ocean remains severely understudied, despite coastal lagoons representing ~13% of the global coastline (Barnes 1980; Santos et al. 2012). This underground lagoon-sea water exchange depends on the hydraulic gradient between the two water bodies (pressure) and the properties of the barrier which separates them, including sediment porosity and permeability. Separately, tides and waves can drive large volumes of seawater into permeable beaches, resulting in a seawater circulation cell (Li et al. 1999; Robinson et al. 2007; Xin et al. 2010). Pore waters from either flow path can obtain a unique geochemical signature from early diagenetic nutrient mineralization (Anschutz et al. 2009; Santos et al. 2009; Charbonnier et al. 2013; Goodridge and Melack 2014) and/or sediment weathering (Schopka and Derry 2012; Ehlert et al. 2016). Lagoon-sea water exchange and seawater circulation flow paths are therefore a potential source of both recycled and new chemical elements to the coastal ocean; thus, it is necessary to understand the time-scale of each flow path to properly evaluate chemical fluxes (Tamborski et al., 2017). Each of these flow paths may be characterized as a type of submarine groundwater discharge (SGD), broadly defined as "any and all flow of water on continental margins from the seabed to the coastal ocean, regardless of fluid composition or driving force" (Burnett et al. 2003).

Lagoon-sea water exchange has been documented along sandy barrier beaches in Fire Island, New York (USA) (Bokuniewicz and Pavlik 1990), Florida Bay (USA) (Corbett et al. 2000; Chanton et al. 2003), Sapelo Island, Georgia (USA) (Evans and Wilson 2017), Malibu Bay, California (USA) (Dimova et al. 2017), Venice Lagoon (Italy) (Rapaglia et al. 2010), Patos-Mirim Lagoon (Brazil) (Windom et al. 2006; Niencheski et al. 2007) and the Great Barrier Reef (Australia) (Santos et al. 2010). Chemical fluxes associated with this SGD have only been

reported for Malibu Bay, Venice Lagoon, Patos-Mirim Lagoon and the Great Barrier Reef (Windom et al. 2006; Niencheski et al. 2007; Rapaglia et al. 2010; Santos et al. 2010; Dimova et al. 2017). All of these study sites are situated along areas with significant tidal ranges to produce water level, and therefore pressure, variations. For example, the tidal range of Venice lagoon (neap = 0.3, spring = 1.2 m), situated along the northern Adriatic Sea, was found to drive SGD flow rates up to 140 cm d^{-1} through highly permeable paleochannels (Rapaglia et al. 2010). However, little to no information exists on the magnitude and temporal variability of this lagoon-sea water exchange flow path to microtidal coastal environments. This is the case of the French Mediterranean coastline, where tides are insignificant (~20 – 30 cm) and there is a striking succession of coastal lagoons of various sizes that are separated from the sea by only narrow sand barriers, constituting ~50% of the coastline (Stieglitz et al. 2013).

Seawater circulation through permeable sandy beaches is primarily driven by tides and waves (Li et al. 1999; Santos et al. 2012) and may be regarded as a net zero water flux. Such a process can induce large volumetric fluxes of circulated seawater in high-energy environments, as observed for example, in Long Island Sound, NY (Tamborski et al., 2017) and the French Aquitanian Coast (Charbonnier et al. 2013). Tides are minor along the French Mediterranean Sea, such that wave-setup and water level fluctuations are hypothesized to drive a net-seaward flowing circulation cell beneath the swash-zone (Sous et al. 2016). The temporal variability of seawater circulation as a vector for solute transport to the French Mediterranean Sea is largely unknown (Tamborski et al. 2018).

The suite of naturally occurring Ra isotopes (^{223}Ra = 11.4 d, ^{224}Ra = 3.66 d, ^{226}Ra = 1,600 y, ^{228}Ra = 5.75 y) and ^{222}Rn (3.83 d) have unique half-lives, which enable tracing pore water flow paths of varying time-scales (Rodellas et al. 2017). These radionuclides are supplied to pore

fluids by the decay of their surface-bound parent isotope through alpha-recoil, and are thus dependent upon sediment grain-size, U/Th content (Porcelli and Swarzenski 2003; Porcelli 2008), and Fe/Mn-oxide surface coatings (Dulaiova et al. 2008; Beck and Cochran 2013). Ra isotopes are primarily adsorbed onto sediment surfaces at low ionic strengths and are partially released into solution at higher ionic strengths due to surface-competition displacement from cations (Webster et al. 1995; Gonneea et al. 2013). Radionuclides can be used in simplified systems to estimate one-dimensional advection or diffusion (horizontal or vertical), when the above-mentioned variables are well-constrained (Krest and Harvey 2003; Smith et al. 2008; Michael et al. 2011).

In this study, we use the term "lagoon-sea water exchange" to refer to the lateral transport of pore waters through a permeable barrier beach, mainly driven by water level differences across the barrier. Separately, we use the term "seawater circulation" to refer to coastal Mediterranean seawater which has been driven into permeable sediments by physical forcing mechanisms, including waves. Using radionuclide tracers and physical observations, we assess the relative magnitude and monthly temporal variability of (1) lagoon-sea water exchange through the barrier beach and (2) seawater circulation through the swash-zone. In addition, we provide a first-order approximation of solute fluxes (DIC, DSi, Ba) driven by these two separate processes.

Study Site

La Palme lagoon is a small coastal lagoon (~500 ha) situated along the French Mediterranean coastline, adjacent to the barrier beach La Franqui (**Figure 1**). The southern basin of La Palme lagoon is a shallow sandy basin (20 – 50 cm water depth) that has limited surface water exchange with the northern basin of the lagoon through a constructed railway dike and bridge and is often partially dry during the summertime. The lagoon may exchange with the

Mediterranean Sea via a small inlet which is naturally opened from high-energy storm-events. Tides in this region are minor (~20 cm), such that when the inlet is closed, water level differences between the southern basin of La Palme lagoon and the Mediterranean Sea are mainly driven by changes in precipitation and evaporation. Precipitation is highest during the fall and spring (440 mm total in 2017); evaporation rates typically exceed precipitation rates during the summer (Stieglitz et al. 2013). The beach sediment of La Franqui is a well-sorted medium sand, with a mean grain-size between 200 – 500 μm.

METHODS

Field Methods

The inlet to the Mediterranean Sea was closed months prior to the start of sampling. A shore-perpendicular transect (T1) was sampled monthly between the southern basin of La Palme lagoon and the Mediterranean Sea during May – September 2017 (**Figure 1**). Transect T1 was additionally sampled in November 2017, four days after the beach was breached by a storm-event, which resumed surficial exchange between the lagoon and the sea. A second transect (T2) was sampled during May 2017 only. Samples along the first transect were evenly spaced 10 m apart; samples from the second transect (~250 m north) were evenly spaced 20 m apart to assess long-shore spatial variability (**Figure 1**).

During May, transects were sampled from boreholes that intersected the saturated zone of the beach; the interstitial water that filled the borehole was immediately sampled. For the remaining sampling campaigns (June – November), pore waters were collected using a shielded-screen (Mesh #50 = 297 μm) drive-point piezometer (Charette and Allen 2006) attached to a vacuum hand pump. Samples were acquired at depth intervals of ~50, 100 and 150 cm below

grade (150 cm for select stations only). Boreholes were dug adjacent to each piezometer sampling location to measure the depth to the water table for all sampling events. During each campaign, lagoon water and Mediterranean Sea surface water endmembers were sampled directly using a hand pump. Salinity, temperature, pH and dissolved oxygen (DO) were immediately measured for all samples in the field using a calibrated WTW hand-probe (Multi 3430). Bulk sediment samples were collected from several boreholes during May 2017 (~50 cm depth). Shore-perpendicular beach topography was surveyed in June 2017 using a real time kinematic GPS (Trimble). We assume that the June 2017 surveyed topography is representative of May, July, August and September, a period in which storms (and thus beach erosion and accretion) were minimal. Beach topography was not surveyed in November 2017.

Analytical Methods

Sediment

Sediment samples were dried at 80 ºC for 48 h and water content loss was measured (triplicate measurements) to calculate sediment porosity, assuming a mineral grain density of 2.65 g cm^{-3} and corrected for sea salt. Bulk sediment samples were sealed for >3 weeks and counted on a semi-planar Canberra Ge detector at 352 keV (^{214}Pb), 583 keV (^{208}Tl) and 911 keV (^{228}Ac) to determine the total (surficial + lattice-bound) activity of solid-phase ^{226}Ra, ^{228}Th and ^{228}Ra, respectively. IAEA 300 and NIST Material 4350B sediment were used to determine the semi-planar detector counting efficiencies.

Sediment samples were additionally measured in a radium delayed coincidence counter (RaDeCC) system (Moore and Arnold 1996), to determine the amount of surface-exchangeable ^{223}Ra and ^{224}Ra produced by ^{227}Th and ^{228}Th present on sediment surfaces (Sun & Torgersen, 1998b). The number of alpha-decays to produce Ra and Rn isotopes are different; this can result

in a slightly different rate of recoil supply of Ra (ϵ) to that of Rn. In the ensuing analyses, we assume $\epsilon = 1.0$ (Krishnaswami et al. 1982, 1991). Therefore, we assume that all ^{219}Rn and ^{220}Rn diffused into the circulating He gas loop of the RaDeCC system are produced by ^{223}Ra and ^{224}Ra decay on sediment surface-exchangeable sites. Radon emanation was measured on the sediment using the column cartridges traditionally used for Mn-fiber measurements. Using the traditional column cartridge, we are able to measure a larger volume of sediment (>150 g) in comparison to the chamber developed by Cai et al. (2012). The disadvantage of the traditional cartridge is that its cylindrical geometry is only suitable for sandy sediment, so that the circulating He gas flow is unobstructed. Fine-grained sediment (silts, clays) could impede the He flow, making this method unusable. Bulk sediment samples were partially dried in an oven until a water:sediment ratio of approximately 0.1 was reached, a ratio previously determined to be sufficient for counting sediment samples on the RaDeCC (Cai et al., 2012; Sun & Torgersen, 1998a). Cartridges were plugged on each end with raw acrylic fiber to prevent any sediment from entering the system. The He flow rate was continuously monitored throughout the measurement period and matched that of typical Mn-fiber measurements (~6 L min^{-1}). A replicate set of homogenized sediment (n = 8) was spiked with 3.8 – 57 dpm ^{224}Ra in equilibrium with ^{228}Th (standard addition; triplicate measurements) to determine the detector counting efficiency (Cai et al., 2012; **Figure 2**). Sediment column ^{224}Ra counting efficiency was equivalent to that of Mn-fiber measurements (Sun & Torgersen, 1998b) and therefore we assume the same detector efficiency as Mn-fiber measurements for both ^{224}Ra and ^{223}Ra. The importance of sample load was tested to determine the effect of helium "channeling" (Cai et al. 2012), with varying sediment loads of 29 – 167 g (n = 7; triplicate measurements).

186 Ra distribution coefficient (K_D) experiments were run on sediment samples from two
187 locations (5-PW5-A and 5-2-PW3-A) to determine the Ra partition coefficient (K) for water
188 salinities of 27 and 38 (representative of salinities measured in beach pore waters), following
189 established protocols for such measurements (e.g. Fisher et al. 1983; Roberts et al. 2009). Briefly,
190 these involve suspending the material of interest (in this case, beach sand) in a solution
191 containing the element for which the distribution coefficient is to be determined, under conditions
192 of in-situ pH and salinity. After equilibration, generally within ~48 h, the fractions of tracer on
193 the sediments and in solution are measured. Sediments were first gamma counted (as noted
194 above) to determine the initial activity of ^{226}Ra from the 352 keV ^{214}Pb photopeak. For each
195 sediment sample, a ^{226}Ra tracer (~20 dpm) was added to 100 mL of Ra-free water containing ~11
196 g (salinity of 27) or ~20 g of sediment (salinity of 38). The pH of each solution was ~7.5 after
197 addition of the ^{226}Ra tracer and no adjustment was made to alter pH for the experiments. Samples
198 were allowed to equilibrate for ~5 days with frequent stirring. At the end of the experiment, the
199 water was decanted off and the sediment was rinsed with small portions of distilled water to
200 remove any residual tracer solution. The sediment was dried and recounted to determine the new
201 ^{226}Ra activity. The activity of ^{226}Ra adsorbed onto the sediment was calculated as the excess
202 ^{226}Ra (above the intrinsic ^{226}Ra activity in the sample) multiplied by the mass of sediment used in
203 the experiment (Eq. 1). K_D was calculated as:

204 $$K_D = \left[\frac{dpm\ ^{226}Ra\ adsorbed}{dpm\ ^{226}Ra\ in\ solution}\right] / C_p \qquad \text{(Eq. 1)}$$

205 where C_p = g sediment per mL of solution. ^{226}Ra was used for these experiments and because the
206 sediments contained natural ^{226}Ra, this fraction was subtracted to determine the partitioning of Ra
207 between solution and solid at the end of the experiment. The solid-phase at the start of the

experiment comprised several fractions of "natural" ^{226}Ra: 1) in the mineral structure, 2) originally adsorbed onto the sediments and 3) originally dissolved in wet sediment pore water (and subsequently adsorbed onto the sediments after drying). All three fractions were effectively measured via the gamma spectrometric measurements of ^{226}Ra before the start of the sorption experiments.

Radium and radon equilibration experiments were also conducted to estimate the production and partitioning of ^{223}Ra, ^{224}Ra and ^{222}Rn from sediments. For ^{223}Ra and ^{224}Ra, ca. 1,000 g of sediment was added into a 6 L plastic container, to which ca. 400 mL of water was added, for a water salinity of 27 and 38 (representative of salinities measured in beach pore waters). The containers were sealed and after >7 weeks the wet sediment was vacuum filtrated to isolate the pore water from the sediment. MnO_2 coated acrylic fibers were subsequently introduced to the extracted solution, partially rinsed, and analyzed on a RaDeCC system, as previously described. For ^{222}Rn, ca. 200 g of dry sediment was added into a 500 mL gas tight bottle, which was then completely filled with Ra-free lagoon water (salinity of 38; triplicates of the same sediment sample were conducted). The bottles were hermetically sealed for >1 month and periodically shaken. The ^{222}Rn concentration in water was measured using the RAD7 coupled to the gas extraction accessory for bottles and corrected to the specific ratio of pore water/solids in sediments following Stieglitz et al. (2013).

Surface & Pore Waters

Between 0.5 – 2 L of pore water was collected for Ra analysis via vacuum hand-pump into plastic containers, for all sampling dates. The plastic containers were left for several hours (or overnight) to allow particles to settle to the bottom of the container. Afterwards, the water overlying the particles was decanted off into a graduated cylinder and volume was recorded; this

231 water was then filtered through raw acrylic fiber (Mn-free) to further remove any particles. In the
232 laboratory, hypoxic (DO < 3 mg L^{-1}) pore water samples were aerated for ~20 minutes; after
233 aeration, Mn-fibers were added directly to the water sample and periodically stirred (< 1 hr) to
234 quantitatively adsorb all Ra from the solution. Two water samples were subjected to a second
235 Mn-fiber addition; these second fibers did not produce any counts (above background) and thus
236 we assume a 100% initial Ra yield. Large volume (> 10 L) endmember samples were
237 traditionally filtered through cartridges (< 1 L min^{-1}). Mn-fibers were triple-rinsed, partially dried
238 (Sun & Torgersen, 1998a) and counted using a RaDeCC to measure the short-lived ^{224}Ra isotope;
239 samples were counted again one week after collection to determine ^{223}Ra (Moore and Arnold
240 1996). Mn-fibers were recounted approximately three weeks after sample collection to measure
241 ^{228}Th, to calculate excess ^{224}Ra (hereafter denoted $^{224}Ra_{ex}$). Detector efficiencies were determined
242 using a ^{232}Th and ^{227}Ac standard; analytical counting uncertainties were calculated by standard
243 rules of error propagation and the results were decay corrected back to the sample collection time
244 (Garcia-Solsona et al. 2008).

245 For ^{222}Rn analysis, pore waters from May, June and November were collected into 250
246 mL air-tight bottles, which were coupled to the piezometer tubing to minimize water-air contact,
247 via vacuum hand-pump. Lagoon and Mediterranean Sea endmembers were collected in 2-L air-
248 tight bottles using a small submersible pump and submerging the bottle beneath the water surface
249 to minimize gas loss. ^{222}Rn samples were analyzed using the radon-in-air monitor RAD7 coupled
250 to a gas extraction accessory for bottles (Durridge Co.) and decay corrected back to the sample
251 collection time; uncertainties are presented as ± 1 standard deviation.

252 Water samples for solute and carbon measurement were syringe filtered using 0.45 μm
253 cellulose acetate filters into rinsed 60 mL PDPE vials. Water samples were diluted 10x with

deionized water and analyzed for dissolved Ba and Si using an ICP-OES (Horiba Jobin Yvon Ultima2®); analytical precision is ≤ 10%. Dissolved inorganic carbon (DIC) and dissolved organic carbon (DOC) were analyzed using a Shimadzu® and results are expressed in molar quantities of carbon; analytical precision is ≤ 5%.

Ancillary Parameters

To investigate the driving mechanisms of seawater circulation through swash-zone, we obtained (1) hourly wind data (speed and direction) from the nearby meteorological station "Leucate" from Météo France, the French meteorological service; and (2) wave sensor data (half-hour intervals) from the nearby buoy "Leucate" (ID 01101) from CEREMA. Wind and waves contribute to local sea-levels and lead to a dynamic interaction between seawater and pore waters. In this study we separate total water levels at the coast into wind and wave contributions as respectively wind-driven setup and wave run-up at the beach. The wind setup formulation (S_{wind}) (Dean and Dalrymple 2004) relates measured wind speeds, direction relative to the shore-normal and distance over which the wind blows (fetch) to a local increase in water levels (Eq. 2) presuming that the wind is present for a long enough time to reach an equilibrium state.

$$S_{wind} = h * \left(\sqrt{1 + \frac{A_S x}{L}} - 1\right) \quad \text{(Eq. 2)}$$

In which A_s is

$$A_s = \frac{2n\tau_s L}{\rho_w g h^2} \quad \text{(Eq. 3)}$$

Where

$$\tau_s = \rho_w c_t W^2 \quad \text{(Eq. 4)}$$

In (Eq. 2), (Eq. 3) and (Eq. 4), h is the mean water depth over the fetch length L, x is the position along the fetch (in this case $x = L$ since we are at the coast), A_s is a dimensionless parameter

containing n, in which $n = 1 - (\tau_b / \tau_s)$ to account for bottom (τ_b) and wind shear stress (τ_s). Here n is set as 1.15, ρ_w represents water density, g is the gravitational acceleration, c_t is a friction coefficient, and W is the wind speed (shore-normal), usually measured at 10 m elevation.

The wave contribution to total sea level at the coast is calculated using a statistical bulk run-up formula (Stockdon et al., 2006). Stockdon et al. (2006) relates offshore measured wave conditions such as significant wave height relative to the shore-normal and peak period to a statistical value for wave run-up (R_{wave}) at the beach (2% exceedance) following:

$$R_{wave} = 1.1 \left(0.35\beta_f \sqrt{H_0 L_0} + \frac{\sqrt{H_0 L_0 \left(0.563\beta_f^2 + 0.004\right)}}{2} \right) \quad \text{(Eq. 5)}$$

Wherein β_f is the beach face slope, H_0 is the offshore wave height (shore-normal) and L_0 represents the offshore wave length. The superposition of the wind and wave contribution results in a time-varying total water level.

The physical impact of wind and waves on seawater circulation in the swash-zone might be far from instantaneous; for example, a certain adaptation time or lag may exist between seawater circulation and the occurring wind and wave conditions. To investigate the importance of this adaptation time lag, mean wind and wave data variables were binned into seven different time-intervals: 2 weeks, 1 week, 72 h, 48 h, 24 h, 12 h and 6 h prior to each sampling. These time intervals were chosen to represent the range in time-scale that is traced by short-lived ^{222}Rn, ^{223}Ra and $^{224}Ra_{ex}$. Binned averages for different wind and wave parameters were compared to radionuclide-derived advection velocities (see Discussion) to investigate any potential temporal variability caused by wind setup and wave setup. Multiple linear regression analysis for uncorrelated variables was performed using XLSTAT 2018.

RESULTS

Sediment

Total (surficial and lattice-bound) ^{226}Ra (0.50 – 0.58 dpm g^{-1}), ^{228}Ra (0.41 – 0.66 dpm g^{-1}), ^{228}Th (0.56 – 0.79 dpm g^{-1}) and sediment porosity (0.38 ± 0.1) showed little variability across the beach transect (**Table 1**). RaDeCC detectors exhibited a linear increase in ^{224}Ra cpm with increasing ^{224}Ra added (solution spike and sediment mass), suggesting that the RaDeCC is suitable for measuring the surface-exchangeable Ra of beach sands (**Figure 2**). Surface-exchangeable Ra was similar between sediment samples, with a mean (± STD; four replicate measurements) activity of 0.0025 ± 0.0002 dpm g^{-1} (n=4) for ^{223}Ra and 0.041 ± 0.006 dpm g^{-1} (n=4) for ^{224}Ra (**Table 2**). Thus, as compared to the bulk ^{228}Th, the recoil efficiency of ^{224}Ra into pore fluid was between ~5 and 7%, as expected for coarse-grained sands (Copenhaver et al. 1993; Porcelli 2008). We assume that all ^{222}Rn input is similar across the beach transect, as evidenced by the solid-phase ^{226}Ra distribution (**Table 1**). The production rate (P; dpm cm^{-3}) of Ra was estimated as

$$P = \frac{(1-\varphi)}{\varphi} * \rho_{sed} * Ra_{surf} \quad \text{(Eq. 6)}$$

Where φ is the sediment porosity (0.38), ρ_{sed} is the grain density (2.65 g cm^{-3}), and Ra_{surf} is the activity of surface-exchangeable Ra (dpm g^{-1}). For the beach transect samples, the production rate (P) with zero partitioning is equal to 10.6 ± 1.0 dpm L^{-1} for ^{223}Ra and 176 ± 25 dpm L^{-1} for ^{224}Ra. The resulting theoretical dissolved equilibrium ^{224}Ra/^{223}Ra activity ratio is thus 16.6 ± 2.8 and is likely not varying across the beach transect (**Table 2**). Note that the difference between the above activities (P) and the actual rate of Ra production (dpm L^{-1} d^{-1}) is simply a function of the Ra isotope decay constant (λ).

Mean K_D values equal 1.7 ± 0.9 $cm^3\ g^{-1}$ at a salinity of 38 (Mediterranean seawater) and 2.7 ± 0.7 $cm^3\ g^{-1}$ at a salinity of 27 (average of two sediment samples; **Table 1**). Considering sediment porosity and grain density, K is equal to 7.5 ± 3.9 at a salinity of 38 and 11.6 ± 3.0 at a salinity of 27 [$K = K_D*\{(1-\varphi)*\rho_{sed}/\varphi\}$]. An estimate can be made of the magnitudes of the pore water ^{226}Ra and adsorbed ^{226}Ra included with the sediments based on the determined K_D values (1.7 – 2.7). For a porosity of 0.38, there was 0.23 $cm^3_{water}/g_{dry\ sediment}$. The experiments used 11 – 20 g of sediment, and the pore water ^{226}Ra in the beach sand was measured as 74 dpm 100 L^{-1}. Pore water ^{226}Ra that would have been present in the two sediment aliquots at the start of the sorption experiments would have been 0.002 and 0.003 dpm, respectively. The in-situ adsorbed ^{226}Ra would have thus been 0.019 and 0.024 dpm for the 11 and 20 g experiments, respectively. Thus, the total ^{226}Ra contributed from dissolved and adsorbed fractions at the start of the experiment was 0.02 – 0.03 dpm. These are small fractions of the total ^{226}Ra activity of the solid phase determined by gamma spectrometry before the K_D experiments (0.5 – 0.6 dpm g^{-1}, or ~6 – 12 dpm total contributed by the 11 – 20 g aliquots) and, as noted above, would have been included in the "starting" ^{226}Ra used to calculate K_D after the sorption experiments (**Table 1**). We also note that the natural "adsorbed" ^{226}Ra would have contributed at most 10% of the sorbed Ra at the conclusion of the K_D experiment, and thus no correction was made for it in calculating K_D. The K_D values measured here (1.7 – 2.7) are comparable to that determined for beach sand by Colbert and Hammond (2008) (K_D = 1.6) and Beck and Cochran (2013) (K_D = 1.14 – 1.60), using a different method.

Sediment incubation experiments represent an equilibrium Ra activity in pore water (production = decay) controlled by the ionic strength of the solution (via K) and may additionally include inputs of Ra from sediment dissolution (i.e. weathering). The equilibrium pore water

342 ^{223}Ra activity was equal to 2.5 ± 0.3 and 3.0 ± 0.2 dpm L^{-1} for a salinity of 27 and 38,
343 respectively; equilibrium $^{224}Ra_{ex}$ activity was equal to 29.0 ± 3.0 and 52.5 ± 4.0 dpm L^{-1} over the
344 same salinity interval, and the resulting ^{224}Ra/^{223}Ra ratios are thus 11.6 ± 1.8 and 17.5 ± 1.8 for
345 salinities of 27 and 38, respectively (**Table 3**). Pore water ^{222}Rn activity in equilibrium with
346 sediments was 160 ± 20 dpm L^{-1} (average of 3 samples).
347 Changes in salinity (ionic strength) drive changes in the partitioning (*K*) of Ra between
348 dissolved and solid-phases (Webster et al. 1995; Gonneea et al. 2008). The activity ratio of
349 mobile ^{224}Ra/^{222}Rn is approximately equivalent to the ratio of the emanation efficiency of ^{222}Rn
350 and the recoil efficiency of ^{224}Ra in fresh groundwater systems when steady-state is achieved
351 (Porcelli and Swarzenski 2003), under the assumption that all alpha-decay radionuclides are
352 supplied at similar rates to that of ^{222}Rn (Krishnaswami et al. 1982). ^{222}Rn is an inert, noble gas
353 whose distribution in pore fluid is supplied chiefly by alpha recoil from sediment surfaces, thus
354 ^{222}Rn is not partitioned between solid and dissolved phases like Ra. Bulk solid-phase ^{228}Th/^{226}Ra
355 activity ratios, the parent isotopes of ^{224}Ra/^{222}Rn, are between 1.05 – 1.37 (**Table 1**); therefore,
356 pore waters in equilibrium with sediment surfaces should have ^{224}Ra/^{222}Rn activity ratios within
357 this range if there is no partitioning of Ra between sediment surfaces and solution. Pore water
358 ^{224}Ra/^{222}Rn activity ratios determined from the equilibration experiments are between 0.18 ± 0.03
359 for a salinity of 27 and 0.33 ± 0.05 for a salinity of 38 (**Table 3**). Assuming that all ^{222}Rn is input
360 at a constant rate and considering a mean surface-exchangeable ^{224}Ra activity of 0.041 ± 0.006
361 dpm g^{-1} (176 ± 25 dpm L^{-1}), then the total (dissolved + surface-bound) ^{224}Ra/^{222}Rn activity ratio is
362 1.28 ± 0.22 for a salinity of 27 and 1.43 ± 0.24 for a salinity of 38 (**Table 3**), approximately
363 within the range of the bulk ^{228}Th/^{226}Ra activity ratios.

General Water Parameters

Precipitation largely occurs during fall and spring months, with little rainfall during the six-month sampling interval (May – November 2017; **Figure 3**). Total precipitation for the week prior to each sampling event equaled 3.4, 0.0, 0.2, 0.2, 2.4 and 0.8 mm for May, June, July, August, September and November, respectively. Wind speed and direction are dominated by two modes, blowing predominantly from either the sea (~90°) towards land or from land (~315°) towards the sea (**Figure 3**). Significant wave height and direction follow a similar pattern to that of wind speed (**Figure 3**).

Lagoon surface water salinity increased between May and September 2017 from 26 to 52, due to low precipitation and high temperatures (**Figure 4**). In May, pore waters sampled between the lagoon and Mediterranean Sea primarily reflected the salinity of the lagoon endmember (26). Pore waters with a slightly lower salinity (~24) were likely derived from past lagoon conditions (April or earlier). During the spring, lagoon water levels were at a maximum (**Table 4**), and the May sampling period therefore experienced the greatest hydraulic gradient between the lagoon and sea, further evidenced by the second transect (T2), sampled over 250 m away (**Figure 4**).

In June and July, pore waters sampled closest to the lagoon were similar in salinity as the lagoon endmember (**Figure 4**). During this time period, pore water salinities decreased continuously with increasing distance from the lagoon towards the sea, reflecting a mixture between recent infiltration of the actual lagoon endmember and older low-salinity (~24) lagoon waters. During August and September, pore waters sampled next to the lagoon were significantly lower in salinity than the lagoon endmember (33 vs. 45 on August 30th; 33 vs. 52 on September 25th). High evaporation rates and low precipitation during August and September (**Figure 3**) resulted in a diminished hydraulic gradient between the lagoon and the sea, corresponding to a

387 period in which lagoon surface water levels were relatively low (**Table 4**). Consequently, the
388 high salinity lagoon waters did not penetrate into the sand barrier during that period, resulting in a
389 large contrast in salinity between the lagoon waters and the pore waters close to the lagoon. In
390 November, strong winds created an opening in the beach spit, forming a natural outlet to the sea,
391 where the barrier beach was approximately half of the width (~40 m) that it had been in previous
392 months. Because of the input of seawater (salinity = 38) into the lagoon, the salinity of the lagoon
393 waters decreased to reach a salinity of 39 (in comparison to 52 in September).

394 ## Radionuclide Distribution

395 Pore waters sampled directly adjacent to the lagoon (1 – 3 m) in May, June and July,
396 which were similar in salinity to that of the lagoon (**Figure 4**), have elevated ^{222}Rn, ^{223}Ra and
397 $^{224}Ra_{ex}$ over the lagoon. This pattern indicates relatively recent lagoon water infiltration and
398 subsequent radionuclide ingrowth from contact with the sediment (**Figures 5 & 6**). ^{222}Rn, ^{223}Ra
399 and $^{224}Ra_{ex}$ activities reach maximum activities within a ~30 m distance from the lagoon. Within
400 the first ~5 – 15 m of the Mediterranean shoreline, pore water salinities reflected that of the
401 Mediterranean Sea (~38), representing a zone in which the beach face was exposed to constant
402 wave-setup. ^{222}Rn, ^{223}Ra, and $^{224}Ra_{ex}$ increased with increasing distance from the shoreline in this
403 seawater salinity zone (**Figure 5**). Vertical profiles show generally increasing activities of pore
404 water ^{222}Rn, ^{223}Ra and $^{224}Ra_{ex}$ with increasing depth, near both the lagoon and the sea (**Figure 7**).

405 In-situ pore water $^{224}Ra/^{222}Rn$ activity ratios were between 0.2 – 0.4 in samples taken in
406 the center of the beach transect (n=14), which are assumed to be in equilibrium with sediment
407 surfaces, since pore water $^{224}Ra/^{222}Rn$ activity ratios determined from the sediment equilibration
408 experiments were 0.18 – 0.33. Considering a mean surface-bound ^{224}Ra activity (0.041 ± 0.006
409 dpm g^{-1}; **Table 2**) and assuming that all labile ^{222}Rn is in solution, then the total (dissolved +

surface-bound) in-situ $^{224}Ra/^{222}Rn$ activity ratio is equal to 2.2 ± 0.7 (n=14). It is important to note that we do not consider ^{222}Rn produced from dissolved ^{226}Ra and any potential absolute differences in the $^{238}U/^{232}Th$ activity ratio of the sediment (Luo et al. 2000).

Dissolved Solutes

DOC was depleted by ~0.1 – 0.4 mM in beach pore waters, with respect to theoretical, two-endmember linear mixing between lagoon surface and Mediterranean Sea endmembers (depending upon position and season; **Figure 8**). Pore water DIC was enriched over both surface endmembers, increasing in concentration toward the center of the beach (**Figure 8**). There was more DIC observed than expected from DOC consumption (~2 – 3 mM), suggesting that there was DIC input to the pore waters from the weathering of carbonate minerals. Consumption of POC (if present in the sand barrier) may also contribute to the DIC enrichment in pore waters. DSi transects were similar to DIC, reaching a relative maximum (100 µM in August) in the center of the beach (**Figure 8**), indicating that dissolution of Si minerals takes place within the sand barrier and releases DSi into the pore water (Anschutz et al. 2009; Tamborski et al. 2018). Vertical DIC and DSi profiles sampled closest to the Mediterranean Sea increased in concentration with increasing depth, similar to ^{222}Rn and $^{223,224}Ra$, for all six sampling seasons (**Figure 7**). Pore waters at 50 cm depth were enriched over surface water concentrations between 25 and 110 µM for DIC, and between 4 and 11 µM for DSi. Transects of dissolved Ba, a chemical analog to Ra, primarily followed two-endmember mixing between surface water endmembers (**Figure 8**), while vertical profiles taken near the sea were relatively constant in concentration with depth (**Figure 7**). Therefore, these profiles suggest that pore water Ra distributions were significantly impacted by ingrowth from water-sediment interaction (**Figure 5**). All surface and pore water data are summarized in the **Supplemental Information**.

DISCUSSION

Reactive-Transport Model

Theory

The change in Ra isotope activity with time may be described with a one-dimensional reactive-transport model. Here we use a horizontal reactive-transport model to describe the Ra activity of the beach transects as a function of advective lagoon-sea water exchange. In parallel, we use a vertical reactive-transport model to describe the Ra activity of the profiles taken adjacent to the Mediterranean Sea, as a function of seawater circulation. Neglecting hydrodynamic dispersion and assuming steady-state conditions (Krest and Harvey 2003; Michael et al. 2011), the advection of Ra in pore water can be described as:

$$A(x) = \frac{P}{1+K} + \left(A_o - \frac{P}{1+K}\right) * e^{-\Delta x \lambda v^{-1}} \quad \text{(Eq. 7)}$$

Where $A(x)$ is the Ra activity (dpm L^{-1}) at distance x (m) from a defined boundary condition, A_o is the initial Ra activity at a $x = 0$, P is the Ra isotope production rate (dpm L^{-1}), K is the dimensionless Ra partition coefficient (adsorbed exchangeable Ra on the solid/dissolved Ra), λ is the Ra isotope decay constant (d^{-1}) and v is the advective pore water velocity (m d^{-1}). Under homogeneous conditions in which groundwater salinity is constant and the initial Ra concentration is zero, Kiro et al. (2012) note that Eq. 7 may be further reduced if $x > \frac{vt}{1+K}$ (where t is time) to:

$$A(x) = \frac{P}{1+K} * (1 - e^{-\Delta x \lambda v^{-1}}) \quad \text{(Eq. 8)}$$

Considering $^{224}Ra_{ex}/^{223}Ra$ activity ratios, the solution to Eq. 7 becomes:

$$\frac{^{224}Ra}{^{223}Ra} = \frac{\frac{P_{224}}{1+K} + \left(A_{224o} - \frac{P_{224}}{1+K}\right) * e^{-\Delta x \lambda_{224} v^{-1}}}{\frac{P_{223}}{1+K} + \left(A_{223o} - \frac{P_{223}}{1+K}\right) * e^{-\Delta x \lambda_{223} v^{-1}}} \quad \text{(Eq. 9)}$$

Equations 7, 8 and 9 may be modeled using a numerical curve-fitting approach, by adjusting the advective velocity term (v) to minimize the root mean square error of the model with respect to the observed data. We have explicitly measured A_o, P (**Table 2**) and K (via K_D and $^{224}Ra/^{222}Rn$ activity ratios; **Tables 1 & 3**) to be used in the model calculations.

$^{224}Ra_{ex}/^{223}Ra$ activity ratios were chosen to model the horizontal advection of lagoon-sea water exchange (Eq. 9). Small-scale sediment heterogeneity may result in variable (equilibrium) pore water ^{223}Ra and ^{224}Ra activity distributions over the ~100 m long beach transects (**Figure 5**). Sediment-exchangeable $^{224}Ra/^{223}Ra$ activity ratios were relatively constant across the beach transect, indicating a homogeneous sediment distribution (**Table 2**); therefore, $^{224}Ra/^{223}Ra$ activity ratios are better suited to identify disequilibrium between pore waters and sediment surfaces (Eq. 9) over absolute activities (Eq. 7 & 8) at such a spatial scale. Here, the horizontal boundary condition is set as the lagoon surface water endmember for May – July, to represent lateral flow through the barrier beach, driven by a positive hydraulic gradient between the lagoon and the sea (**Table 4**). We cannot assume steady-state conditions for August – September (because of the diminished hydraulic gradient) and November (the spit was recently breached); therefore, we do not model these months. The horizontal model is limited to shallow pore water samples only, where we could collect sediment samples. Shallow pore water samples closest to the lagoon are lower in ^{223}Ra and $^{224}Ra_{ex}$ activity compared to deeper samples (**Figure 7**); therefore, we consider these shallow samples as representative of this active water exchange zone, here defined as 1.0 m depth.

To estimate seawater circulation in the swash-zone, radionuclide activities were modeled for the pore water profiles sampled closest to the Mediterranean Sea (A_o) (Eq. 7), where pore water salinities were equivalent to seawater (**Figure 7**). The vertical advective velocity is a rate of flushing exchange (net zero water flux), in which Ra atoms are lost from pore waters, similar to pore water exchange creating a (total) ^{224}Ra deficit relative to its surface-bound parent ^{228}Th (Cai et al. 2014), but here we only consider the dissolved Ra pool. The short-lived radionuclide flux is not necessarily driven by a net water (discharge or recharge) flux; rather, the Ra flux can be sustained by seawater circulation (net zero water flux) (Cook et al. 2018a). The deficit of short-lived ^{222}Rn, ^{223}Ra and $^{224}Ra_{ex}$ does not reflect instantaneous seawater circulation for the exact time of sampling; rather, the radionuclide deficit is integrating across the time-scale of radionuclide ingrowth and decay. $^{224}Ra_{ex}/^{223}$Ra activity ratios were not used for the vertical model because the range of the ^{224}Ra/^{223}Ra activity ratios (and its relative uncertainty) were much lower compared to the larger range in activity ratio observed for the horizontal transects (~10 – 35). Terms used in the one-dimensional horizontal and vertical reactive transport models are summarized in **Table 5**.

Sensitivity & Assumptions

Reactive-transport model sensitivity to changes in production rate (P) and Ra partition coefficient (K; or the "retardation factor" $R = 1 + K$) have been summarized in detail elsewhere (Tricca et al. 2001; Krest and Harvey 2003; Michael et al. 2011; Kiro et al. 2015; Tamborski et al. 2017). Michael et al. (2011) note that the ratio of Ra production to retardation is difficult to quantify and should be done so carefully in order to use the one-dimensional reactive-transport model in any quantitative, meaningful way. Tamborski et al. (2017) showed that radionuclide-derived pore water residence times ($\tau = v/d$) within tidal beach environments are sensitive to

497 values of P for long residence times, but less sensitive when residence times are low
498 (approximately less than one day). It is important to note that flow velocity is spatially and
499 temporally variable, and is not as simple as the depiction of the one-dimensional model due to
500 subsurface heterogeneity (Michael et al. 2011).

501 Sediment equilibration-derived K values (from $^{224}Ra/^{222}Rn$; **Table 3**) for two different
502 salinity solutions (27 and 38) were not significantly different when considering surface-bound
503 ^{224}Ra, with respect to their range in uncertainties. In-situ determined K values (2.2 ± 0.7) were
504 slightly higher than those determined from the sediment equilibration experiments and exhibited
505 greater variability, as evidenced by a large standard deviation. All K values estimated from
506 $^{224}Ra/^{222}Rn$ activity ratios are lower than experimentally determined values from the sorption
507 experiments (7.5 – 11.6). This discrepancy may be explained by an experimental particle
508 concentration effect, as observed for the highly particle-reactive ^{234}Th (Honeyman et al. 1988). In
509 theory, K_D should remain constant regardless of the particle-to-solution ratio used
510 experimentally; in practice, measured K_D values are greater for experiments with smaller particle-
511 to-solution ratios, which can result in a factor of ~10 difference in K_D (Honeyman et al. 1988). In-
512 situ particle-to-solution ratios are an order of magnitude greater than particle-to-solution ratios
513 typically used for K_D experiments. Indeed, Cochran et al. (1986) determined that the K_D for Th
514 was $\sim 10^5$ cm^3 g^{-1} in nearshore (Buzzards Bay, MA, USA) sediment pore waters, in contrast to
515 values two orders of magnitude greater ($\sim 10^7$ cm^3 g^{-1}) in the deep sea (Bacon and Anderson
516 1982; Honeyman et al. 1988).

517 Considering the range in K values noted above, we elect to use values derived from in-situ
518 $^{224}Ra/^{222}Rn$ activity ratios for samples assumed to be in equilibrium with sediment surfaces, taken
519 in the center of the beach transect (2.2 ± 0.7; n=14). We use a range in K determined from the
520 standard deviation, to represent a minimum K (1.5) for salinity 38 and a maximum K (2.9) for

521 salinity 27. This range in K is qualitatively validated from the sorption K_D experiments (despite
522 the particle-concentration effect noted above), which provides additional confidence to this
523 approach. The uncertainty of the sediment equilibration K values prevents us from accurately
524 distinguishing between salinities of 27 and 38, despite observable differences in experimental
525 (**Table 3**) and in-situ (**Figure 5**) dissolved ^{223,224}Ra activities.

526 Ra desorption from estuarine sediments is a non-linear process chiefly governed by the
527 availability of Ra on particle surfaces and the major ion present in solution, where non-linearity is
528 typically greatest between a salinity of 0 and ~15 (Webster et al. 1995). Changes between K and
529 salinity for relatively high ionic strength solutions (i.e. > 30% seawater composition for seawater
530 salinity of 36) may be approximated as linear (Webster et al. 1995; Kiro et al. 2012, 2013). Here
531 we assume a linear relationship between K and salinity along the horizontal groundwater flow
532 path for salinity 27 (K = 2.9) and salinity 38 (K = 1.5), based on the observed pore water salinity
533 distribution (**Figure 4**). We further extrapolate to a salinity of 22 and 42 to match the observed
534 minimum and maximum salinity. Bulk ^{228}Th (**Table 1**) and surface-exchangeable ^{224}Ra (**Table 2**)
535 are relatively uniform throughout the beach. We assume that the mean value of P is
536 representative of the beach transect in the horizontal direction. Values of P were measured for
537 surficial sediments (~0 – 50 cm depth) along the investigated transect; values of P may change
538 with depth in the vertical model due to differing amounts of ^{228}Th present on sediment surfaces.
539 Spatially variable Ra and Rn production can occur if there are significant differences in the Fe
540 and Mn (hydr)oxide coatings on sediment surfaces (Dulaiova et al. 2008; Beck and Cochran
541 2013), or barite ($BaSO_4$) precipitation (Kiro et al. 2012), which we do not consider at present. For
542 the vertical reactive-transport model, the term $[P/(1+K)]$ is simply constrained from the sediment
543 incubation experiments for seawater salinity (**Table 3**).

544 ***Model Results***

545 Results from the horizontal model (Eq. 9) for lagoon-sea water exchange are presented in
546 **Figure 9**. In general, there was an abrupt increase in the observed $^{224}Ra_{ex}/^{223}Ra$ activity ratio
547 within a few meters of the lagoon boundary, due to the relatively more rapid ingrowth of ^{224}Ra
548 with respect to ^{223}Ra, followed by an abrupt decrease in the activity ratio, in which ^{224}Ra reached
549 equilibrium with sediment-surfaces while ^{223}Ra continued to be produced, until the dissolved
550 activity of both isotopes was balanced by production and decay ($^{224}Ra_{ex}/^{223}Ra$ = 16.7; **Table 2**).
551 Model best-fit horizontal advective velocities decreased from 85 to 30 to 20 cm d^{-1} for May, June
552 and July, respectively (**Figure 9**), following the decreasing hydraulic gradient (**Table 4**). The two
553 transects sampled in May (over 250 m apart) have equal advective velocities from the modeled
554 $^{224}Ra_{ex}/^{223}Ra$ activity ratios, suggesting that the flow of lagoon water through the beach was
555 prevalent along La Palme lagoon and the beach of La Franqui during this high-water level period.
556 Therefore, during May, pore water residence times were on the order of hours close to the lagoon
557 edge (~1 m), several days within 10 m of the lagoon and several weeks in the center of the beach.
558 Advective linear velocities are converted to water fluxes considering a mean sediment porosity of
559 0.38 (**Table 5**) and an exchange zone depth of 1.0 m (**Figure 7**). Volumetric water fluxes for
560 May, June and July are therefore between 0.1 – 0.3 m^3 d^{-1} m^{-1} of shoreline.

561 We can qualitatively compare our horizontal one-dimensional reactive-transport model
562 results to the observed changes in pore water salinity with time (**Figure 4**). Changes in pore water
563 salinity are explained by mixing between current high-salinity lagoon waters and older (fresher)
564 lagoon waters, driven laterally toward the sea from a positive hydraulic gradient (**Table 4**). The
565 pore water salinity profile observed on June 22nd persisted 14 days later to July 6th, as the lagoon
566 water level decreased (**Table 4**) and increased in salinity (37 to 39). On July 6th, the lower
567 salinity endmember from May (~25) was observed up to 42 m away from the lagoon, an absolute

568 difference of 6 m (seaward) from June 22nd. The difference in the lower salinity plumes
569 horizontal position across the beach corresponds to an integrated horizontal flow velocity of ~43
570 cm d^{-1} (6 m/14 d). From August 30th to September 25th the low salinity plume reversed direction;
571 the plume was displaced 11 m toward the lagoon (~40 cm d^{-1}).

572 Vertical profiles (Eq. 7; derived from ^{223}Ra) displayed significant temporal variability,
573 with model best-fit vertical advective velocities equal to 30, 14, 10, 25, 55 and 52 cm d^{-1} for May,
574 June, July, August, September and November, respectively (e.g. **Figure 10**). Estimates derived
575 from ^{222}Rn equal 30 and 90 cm d^{-1} for June and November (**Figure 10**), in relative agreement
576 with ^{223}Ra, despite integrating over different time-scales. $^{224}Ra_{ex}$ model results are linearly
577 correlated to estimates from ^{223}Ra (slope = 0.92). Scaling the ^{223}Ra best-fit vertical advective
578 velocities to the width of the swash-zone impacted by seawater circulation (5 m into the beach-
579 face and 5 m into the sea) and considering a mean porosity of 0.38 results in volumetric seawater
580 circulation fluxes between 0.4 – 2.1 m^3 d^{-1} m^{-1} of shoreline. We note that the seawater circulation
581 fluxes for September and November may easily be a factor of two larger, considering the width
582 of the beach impacted by wave-setup, from the observed pore water salinity distribution (**Figure**
583 **4**).

584 The Mediterranean beach studied here has a minor tidal range (~20 – 30 cm); therefore,
585 we can compare the above results to other studies conducted in areas with significant tidal ranges
586 to qualitatively assess the role of tidal pumping as a driver of both lagoon-sea water exchange
587 and seawater circulation. Lagoon-sea water exchange fluxes (0.1 – 0.3 m^3 d^{-1} m^{-1} of shoreline)
588 are an order of magnitude lower than those obtained from higher-energy tidal environments
589 subject to exchange through a permeable barrier (e.g. 2.6 – 5.7 m^3 m^{-1} of shoreline per tide for
590 Cabretta Beach, Georgia) (Evans and Wilson 2017). The advective linear velocity estimated for
591 May is similar to rates in a porous limestone coral-reef environment (100 cm d^{-1}) (Santos et al.

2010). Larger tidal ranges produce greater water level differences between coastal lagoons and the coastal sea, effectively increasing the hydraulic gradient and therefore SGD rate.

The volumetric flux of seawater circulation estimated here for the swash-zone (0.4 – 2.1 $m^3\ d^{-1}\ m^{-1}$ of shoreline) is lower than modeling estimates of wave-swash induced infiltration to the unsaturated zone of a sandy beach (1.6 $m^3\ m^{-1}$ of shoreline per tidal cycle) (Heiss et al. 2014), and is an order of magnitude lower than the highly energetic Aquitanian French coastline (~15.2 $m^3\ m^{-1}$ of shoreline per tidal cycle), driven by tidal pumping and wave-setup (Charbonnier et al. 2013). Large tidal variations drive greater amounts of seawater into permeable sediments; tidal pumping is likely more significant than wave or wind-setup in tidal environments with limited fetch (Bokuniewicz et al. 2015).

Physical Drivers of Exchange

Lagoon-Sea Water Exchange

Lagoon-sea water exchange is driven by the pressure induced hydraulic gradient between the water level of the lagoon and the water level of the Mediterranean Sea. It is apparent that as the lagoon water level decreased from spring through summer, the hydraulic gradient between the lagoon and the Mediterranean Sea decreased (**Table 4**), resulting in a slower flow of water through the beach. Qualitative flow estimates from Darcy's law ($Q = -k_h * i$), considering a hydraulic conductivity (k_h) on the order of 10^{-2} to 10^{-3} m s^{-1} for clean sands (Freeze and Cherry, 1979) and the hydraulic gradient between the lagoon and the sea (i; **Table 4**) results in horizontal flow velocities on the order of ~100 cm d^{-1}. The absolute value of the Darcy flux should not be overly interpreted here, as we do not have detailed information on water table elevation (few point measurements) and sediment hydraulic conductivity (assumed values). Nevertheless, this

exercise is useful to constrain the relative magnitude of the horizontal flow velocity to that of the horizontal reactive-transport model.

Seawater Circulation

Vertical flushing velocities were highly variable over the six-month sampling campaign (**Figure 10**). Variability in vertical flushing can change with wave height, wave period and wave direction, all of which are a function of the prevailing wind speed and direction. According to the results from the multiple linear-regression model (Section *Ancillary Parameters*), wind speed and direction significantly explain the temporal variability in vertical flushing velocities. Regression coefficients are strongest for the 48 h and 72 h binned averages ($R^2 = 0.87$ and 0.92, $F = 0.02$ and 0.05, $df = 3$) (**Table 6**). Regression coefficients are weaker for the 6 – 24 h binned averages ($R^2 = 0.64 – 0.79$, $F \geq 0.1$, $df = 3$); no correlation is observed for the 1-week and 2-week binned averages ($R^2 = 0.2$). The significant relationships over the 48 and 72 h intervals display the "memory effect" that Ra and Rn isotopes have in integrating water exchange fluxes over the time-scale of the radionuclide half-life. In contrast, wind-setup and wave-runup (Eq. 2 – 5) significantly explain the temporal variability in vertical flushing for only the 6 h binned average ($R^2 = 0.87$, $F = 0.05$, $df = 3$) (**Table 6**). Several hours may be needed for winds to produce waves in the Mediterranean Sea; however, only a few hours may be needed for waves to affect pore waters, both of which are highly dependent upon direction.

Biogeochemical Significance

Lagoon-sea water exchange and seawater circulation flow paths drive early diagenetic nutrient mineralization (Charbonnier et al. 2013) and sediment weathering reactions (Ehlert et al. 2016). Here we provide a first-order estimate of solute fluxes driven by lagoon-sea water exchange during high water conditions, assuming that flow through the barrier beach was

637 ultimately supplied to the Mediterranean Sea. Lagoon-sea water exchange is a net water source
638 and may therefore be a net solute flux to the coastal Mediterranean Sea, depending upon
639 biogeochemical reactions (Cook et al. 2018b). Solute concentrations measured at ~20 m distance
640 from the sea (**Table 7**) are used as the endmember to estimate lagoon-sea water exchange solute
641 fluxes. At this distance, we assume negligible dilution from mixing with seawater (**Figure 4**) and
642 that most of the biogeochemical transformations have occurred (**Figure 8**). Corresponding DSi,
643 DIC and Ba fluxes equal 10 mmol Si d^{-1} m^{-1}, 1,100 mmol C d^{-1} m^{-1} and 70 μmol Ba d^{-1} m^{-1} of
644 shoreline during May 2017 (**Table 7**). Solute fluxes decrease from June to July (**Table 7**) as a
645 consequence of reduced flow (**Figure 9**).

646 The lagoon-sea water exchange DIC flux is ~70 – 200 mmol m^{-2} d^{-1} assuming a 5 m wide
647 seepage-face; this flux is within the global range of DIC inputs from SGD (~10 – 2000 mmol m^{-2}
648 d^{-1}) summarized by Sadat-Noori et al. (2016). DIC inputs from lagoon-sea water exchange can
649 lead to coastal ocean acidification (Robinson et al. 2018), which may explain the relatively low
650 pH values measured in the coastal Mediterranean Sea during the spring (pH = 8.03 in May, pH =
651 8.20 in June and pH = 8.25 in September; **Supplemental Information**). With regard to Ba,
652 dissolved concentrations are typically ~40 nM in the Mediterranean Sea (Jacquet et al. 2016).
653 Local Ba inputs from lagoon-sea water exchange may alter local Ba biogeochemical cycling;
654 further work is required to understand the role of SGD as a source of Ba to the Mediterranean
655 Sea.

656 Adjacent to the Mediterranean Sea, pore waters with the same salinity as seawater were
657 enriched in DIC (25 – 110 μM C) and DSi (4 – 11 μM Si) over surface waters, while Ba
658 concentrations were relatively uniform (**Figure 7**). Linear Ba profiles suggest that seawater
659 circulation in the swash-zone is not a net source of Ba to the coastal sea. We may estimate solute

660 fluxes in the swash-zone by multiplying the net solute concentration (enrichment over
661 Mediterranean seawater) by the volume of seawater circulation (Cook et al. 2018b). Seawater
662 circulation-driven DIC fluxes through the swash-zone are between 14 – 220 mmol C d^{-1} m^{-1} of
663 shoreline (**Table 7**), possibly as a consequence of carbonate mineral weathering, in addition to
664 POC and DOC consumption (**Figure 7**). Seawater circulation-driven DSi fluxes through the
665 swash-zone are between 3 – 8 mmol Si d^{-1} m^{-1} of shoreline (**Table 7**).
666 During November 2016, SGD was estimated to supply a DSi flux of 2.4 ± 1.4 mol Si d^{-1}
667 m^{-1} of shoreline for La Franqui, based on offshore transects that were conducted in the coastal
668 seas (Tamborski et al. 2018). This DSi flux was hypothesized to be driven by both lagoon-sea
669 water exchange (relatively high-water levels) and seawater circulation (Tamborski et al. 2018);
670 this flux is 2 – 3 orders of magnitude larger than the DSi fluxes calculated here for the swash-
671 zone (**Table 7**). The DSi flux of Tamborski et al. (2018) may include additional, unaccounted for
672 flow paths between the swash-zone (this study) and 300 m offshore, where the surface water
673 transects to quantify SGD originated (Figure 6 of Tamborski et al., 2018). Water depth is ≤ 5 m
674 over 300 m from shore; seawater circulation through this shallow zone, over a large area (~3
675 km^2), may thus be an adequate source of DSi (and Ra) offshore of La Franqui. To reconcile the
676 difference in the DSi flux from this study and Tamborski et al. (2018), we hypothesize that
677 offshore seawater circulation may supply a DSi flux on the order of 1 – 2 mol Si d^{-1} m^{-1} of
678 shoreline. While seawater circulation is relatively small in supplying DSi from the narrow swash-
679 zone, this flow path may be significant over the larger area of the shallow coastal zone; future
680 research is required to better constrain these coastal solute fluxes.

CONCLUSIONS

Various flow paths make up the term submarine groundwater discharge (SGD) (Santos et al. 2012). Individual driving mechanisms are seldom quantified with respect to absolute water fluxes and its associated chemical load to the sea (Robinson et al. 2018), despite increasing recognition that individual flow paths may have unique geochemical signatures (Tamborski et al. 2017; Rodellas et al. 2018). In this study we present a simple Ra isotope methodology, which builds upon preexisting analytical measurements and theoretical models to explicitly quantify (1) lagoon-sea water exchange through a permeable sand barrier and (2) seawater circulation in the swash-zone of the sand barrier. Multiple methods are recommended to determine the production (P) and partitioning (K) of Ra between sediment surfaces and solution in order to properly model 1-D Ra transport. This methodology provides a framework where future researchers may discriminate between unique SGD flow paths, which in turn will help improve solute flux estimates and our understanding of coastal biogeochemical cycles.

Repeated measurements at a Mediterranean barrier beach site show that lagoon-sea water exchange varies in response to the changing hydraulic gradient between the lagoon and the sea. This flow path is a net water flux which supplies the greatest DSi (10 mmol d^{-1} m^{-1}), DIC (1,100 mmol d^{-1} m^{-1}) and Ba (70 µmol d^{-1} m^{-1}) flux to the coastal Mediterranean Sea during high lagoon water-level periods. The DIC flux from lagoon-sea water exchange is comparable to other SGD studies and suggests that this vector may enhance coastal ocean acidification in the Mediterranean Sea (Sadat-Noori et al. 2016). We conclude that coastal lagoons represent a significant source of new DIC and Ba to the Mediterranean Sea during high water-level periods and are likely an important source for other dissolved chemical elements as well. Solute fluxes may significantly decrease during the dry season (summer), when lagoon surface water-levels

decrease. As a result, this seasonal vector should be considered in future coastal zone chemical budgets.

Seawater circulation through the swash-zone varies in response to short-term (hours to days) changes in regional wind and wave regimes. This is one of the first studies to quantitatively link a seawater circulation flux to its physical driving mechanism(s), tidal pumping notwithstanding. This vector is relatively minor in transferring DSi and DIC to the Mediterranean Sea during the studied period (May – November 2017), while Ba inputs are negligible. It remains to be seen how significant these individual flow paths are in transferring other chemical elements, such as N and P, to the coastal Mediterranean Sea. Further work is required to understand the importance of seawater circulation along the shallow nearshore coastal zone (~0 – 300 m offshore) to the Mediterranean Sea.

REFERENCES

Anschutz, P., T. Smith, A. Mouret, J. Deborde, S. Bujan, D. Poirier, and P. Lecroart. 2009. Tidal sands as biogeochemical reactors. Estuar. Coast. Shelf Sci. **84**: 84–90. doi:10.1016/j.ecss.2009.06.015

Bacon, M. P., and R. F. Anderson. 1982. Distribution of thorium isotopes between dissolved and particulate forms in the deep sea. J. Geophys. Res. **87**: 2045. doi:10.1029/JC087iC03p02045

Barnes, R. S. K. 1980. Coastal Lagoons, Cambridge University Press.

Beck, A. J., and M. A. Cochran. 2013. Controls on solid-solution partitioning of radium in saturated marine sands. Mar. Chem. **156**: 38–48. doi:10.1016/j.marchem.2013.01.008

Bokuniewicz, H., J. K. Cochran, J. Garcia-Orellana, V. Rodellas, J. W. Daniel, and C. Heilbrun. 2015. Intertidal percolation through beach sands as a source of 224.223Ra to Long Island Sound, New York and Connecticut, United States. J. Mar. Res. **73**: 123–140. doi:10.1357/002224015816665570

Bokuniewicz, H., and B. Pavlik. 1990. GROUNDWATER SEEPAGE ALONG A BARRIER-ISLAND. Biogeochemistry **10**: 257–276.

Burnett, W. C., H. Bokuniewicz, M. Huettel, W. S. Moore, and M. Taniguchi. 2003. Groundwater and pore water inputs to the coastal zone. Biogeochemistry **66**: 3–33. doi:10.1023/B:BIOG.0000006066.21240.53

733 Cai, P., X. Shi, W. S. Moore, and M. Dai. 2012. Measurement of 224Ra:228Th disequilibrium in
734 coastal sediments using a delayed coincidence counter. Mar. Chem. **138**–**139**: 1–6.
735 doi:10.1016/j.marchem.2012.05.004

736 Cai, P., X. Shi, W. S. Moore, S. Peng, G. Wang, and M. Dai. 2014. 224Ra:228Th disequilibrium
737 in coastal sediments: Implications for solute transfer across the sediment-water interface.
738 Geochim. Cosmochim. Acta **125**: 68–84. doi:10.1016/j.gca.2013.09.029

739 Chanton, J., W. Burnett, H. Dulaiova, D. Corbett, and M. Taniguchi. 2003. Seepage rate
740 variability in Florida Bay driven by Atlantic tidal height. Biogeochemistry **66**: 187–202.

741 Charbonnier, C., P. Anschutz, D. Poirier, S. Bujan, and P. Lecroart. 2013. Aerobic respiration in
742 a high-energy sandy beach. Mar. Chem. **155**: 10–21. doi:10.1016/j.marchem.2013.05.003

743 Charette, M. A., and M. C. Allen. 2006. Precision ground water sampling in coastal aquifers
744 using a direct-push, shielded-screen well-point system. Gr. Water Monit. Remediat. **26**: 87–
745 93. doi:10.1111/j.1745-6592.2006.00076.x

746 Cochran, J. K., A. E. Carey, E. R. Sholkovitz, and L. D. Surprenant. 1986. The geochemistry of
747 uranium and thorium in coastal marine sediments and sediment pore waters. Geochim.
748 Cosmochim. Acta **50**: 663–680. doi:10.1016/0016-7037(86)90344-3

749 Colbert, S. L., and D. E. Hammond. 2008. Shoreline and seafloor fluxes of water and short-lived
750 Ra isotopes to surface water of San Pedro Bay, CA. Mar. Chem. **108**: 1–17.
751 doi:10.1016/j.marchem.2007.09.004

752 Cook, P. G., V. Rodellas, A. Andrisoa, and T. C. Stieglitz. 2018a. Exchange across the sediment-
753 water interface quantified from porewater radon profiles. J. Hydrol. **559**: 873–883.
754 doi:10.1016/J.JHYDROL.2018.02.070

755 Cook, P. G., V. Rodellas, and T. C. Stieglitz. 2018b. Quantifying Surface Water, Porewater, and
756 Groundwater Interactions Using Tracers: Tracer Fluxes, Water Fluxes, and End-member
757 Concentrations. Water Resour. Res. **54**: 2452–2465. doi:10.1002/2017WR021780

758 Copenhaver, S. A., S. Krishnaswami, K. K. Turekian, N. Epler, and J. K. Cochran. 1993.
759 RETARDATION OF U-238 AND TH-232 DECAY CHAIN RADIONUCLIDES IN
760 LONG-ISLAND AND CONNECTICUT AQUIFERS. Geochim. Cosmochim. Acta **57**:
761 597–603. doi:10.1016/0016-7037(93)90370-c

762 Corbett, D. R., K. Dillon, and W. Burnett. 2000. Tracing groundwater flow on a barrier island in
763 the north-east Gulf of Mexico. Estuar. Coast. Shelf Sci. **51**: 227–242.

764 Dean, R. G., and R. A. Dalrymple. 2004. Coastal Processes with Engineering Applications,
765 Cambridge University Press.

766 Dimova, N., P. Ganguli, P. Swarzenski, J. Izbicki, and D. O'Leary. 2017. Hydrogeologic controls
767 on chemical transport at Malibu Lagoon, CA: Implications for land to sea exchange in
768 coastal lagoon systems. J. Hydrol. Reg. Stud. **11**: 219–233. doi:10.1016/j.ejrh.2016.08.003

769 Dulaiova, H., M. E. Gonneea, P. B. Henderson, and M. A. Charette. 2008. Geochemical and

770 physical sources of radon variation in a subterranean estuary - Implications for groundwater
771 radon activities in submarine groundwater discharge studies. Mar. Chem. **110**: 120–127.
772 doi:10.1016/j.marchem.2008.02.011

773 Ehlert, C., A. Reckhardt, J. Greskowiak, B. T. P. Liguori, P. Boning, R. Paffrath, H. J. Brumsack,
774 and K. Pahnke. 2016. Transformation of silicon in a sandy beach ecosystem: Insights from
775 stable silicon isotopes from fresh and saline groundwaters. Chem. Geol. **440**: 207–218.
776 doi:10.1016/j.chemgeo.2016.07.015

777 Evans, T. B., and A. M. Wilson. 2017. Submarine groundwater discharge and solute transport
778 under a transgressive barrier island. J. Hydrol. **547**: 97–110.
779 doi:10.1016/J.JHYDROL.2017.01.028

780 Fisher, N. S., P. Bjerregaard, and S. W. Fowler. 1983. Interactions of marine plankton with
781 transuranic elements. 1. Biokinetics of neptunium, plutonium, americium, and californium in
782 phytoplankton. Limnol. Oceanogr. **28**: 432–447. doi:10.4319/lo.1983.28.3.0432

783 Freeze, R. A., and J. A. C. N.-R. Cherry VA Menlo Park, CA Flagstaff, AZ Denver, CO. 1979.
784 Groundwater, Prentice-Hall.

785 Garcia-Solsona, E., J. Garcia-Orellana, P. Masque, and H. Dulaiova. 2008. Uncertainties
786 associated with Ra-223 and Ra-224 measurements in water via a Delayed Coincidence
787 Counter (RaDeCC). Mar. Chem. **109**: 198–219. doi:10.1016/j.marchem.2007.11.006

788 Gonneea, M. E., P. J. Morris, H. Dulaiova, and M. A. Charette. 2008. New perspectives on
789 radium behavior within a subterranean estuary. Mar. Chem. **109**: 250–267.
790 doi:10.1016/j.marchem.2007.12.002

791 Gonneea, M. E., A. E. Mulligan, and M. A. Charette. 2013. Seasonal cycles in radium and barium
792 within a subterranean estuary: Implications for groundwater derived chemical fluxes to
793 surface waters. Geochim. Cosmochim. Acta **119**: 164–177. doi:10.1016/j.gca.2013.05.034

794 Goodridge, B. M., and J. M. Melack. 2014. Temporal evolution and variability of dissolved
795 inorganic nitrogen in beach pore water revealed using radon residence times. Environ. Sci.
796 Technol. **48**: 14211–14218. doi:10.1021/es504017j

797 Heiss, J. W., W. J. Ullman, and H. A. Michael. 2014. Swash zone moisture dynamics and
798 unsaturated infiltration in two sandy beach aquifers. Estuar. Coast. Shelf Sci. **143**: 20–31.
799 doi:10.1016/J.ECSS.2014.03.015

800 Honeyman, B. D., L. S. Balistrieri, and J. W. Murray. 1988. Oceanic trace metal scavenging: the
801 importance of particle concentration. Deep Sea Res. Part A. Oceanogr. Res. Pap. **35**: 227–
802 246. doi:10.1016/0198-0149(88)90038-6

803 Jacquet, S. H. M., C. Monnin, V. Riou, L. Jullion, and T. Tanhua. 2016. A high resolution and
804 quasi-zonal transect of dissolved Ba in the Mediterranean Sea. Mar. Chem. **178**: 1–7.
805 doi:10.1016/J.MARCHEM.2015.12.001

806 Kiro, Y., Y. Weinstein, A. Starinsky, and Y. Yechieli. 2013. Groundwater ages and reaction rates
807 during seawater circulation in the Dead Sea aquifer. Geochim. Cosmochim. Acta **122**: 17–

35. doi:10.1016/j.gca.2013.08.005

Kiro, Y., Y. Weinstein, A. Starinsky, and Y. Yechieli. 2015. Application of radon and radium isotopes to groundwater flow dynamics: An examples from the Dead Sea. Chem. Geol. **411**: 155–171. doi:10.1016/j.chemgeo.2015.06.014

Kiro, Y., Y. Yechieli, C. I. Voss, A. Starinsky, and Y. Weinstein. 2012. Modeling radium distribution in coastal aquifers during sea level changes: The Dead Sea case. Geochim. Cosmochim. Acta **88**: 237–254. doi:10.1016/j.gca.2012.03.022

Krest, J. M., and J. W. Harvey. 2003. Using natural distributions of short-lived radium isotopes to quantify groundwater discharge and recharge. Limnol. Oceanogr. **48**: 290–298.

Krishnaswami, S., R. Bhushan, and M. Baskaran. 1991. Radium isotopes and 222Rn in shallow brines, Kharaghoda (India). Chem. Geol. Isot. Geosci. Sect. **87**: 125–136. doi:10.1016/0168-9622(91)90046-Y

Krishnaswami, S., W. C. Graustein, K. K. Turekian, and J. F. Dowd. 1982. RADIUM, THORIUM AND RADIOACTIVE LEAD ISOTOPES IN GROUNDWATERS - APPLICATION TO THE INSITU DETERMINATION OF ADSORPTION-DESORPTION RATE CONSTANTS AND RETARDATION FACTORS. Water Resour. Res. **18**: 1663–1675. doi:10.1029/WR018i006p01663

Li, L., D. A. Barry, F. Stagnitti, and J. Y. Parlange. 1999. Submarine groundwater discharge and associated chemical input to a coastal sea. Water Resour. Res. **35**: 3253–3259.

Luo, S., T.-L. Ku, R. Roback, M. Murrell, and T. McLing. 2000. In-situ radionuclide transport and preferential groundwater flows at INEEL (Idaho): decay-series disequilibrium studies. Geochim. Cosmochim. Acta **64**: 867–881.

Michael, H. A., M. A. Charette, and C. F. Harvey. 2011. Patterns and variability of groundwater flow and radium activity at the coast: A case study from Waquoit Bay, Massachusetts. Mar. Chem. **127**: 100–114. doi:10.1016/j.marchem.2011.08.001

Moore, W. S., and R. Arnold. 1996. Measurement of Ra-223 and Ra-224 in coastal waters using a delayed coincidence counter. J. Geophys. Res. **101**: 1321–1329. doi:10.1029/95JC03139

Niencheski, L. F. H., H. L. Windom, W. S. Moore, and R. A. Jahnke. 2007. Submarine groundwater discharge of nutrients to the ocean along a coastal lagoon barrier, Southern Brazil. Mar. Chem. **106**: 546–561. doi:10.1016/j.marchem.2007.06.004

Porcelli, D. 2008. Chapter 4 Investigating Groundwater Processes Using U- and Th-Series Nuclides. Radioact. Environ. **13**: 105–153. doi:10.1016/S1569-4860(07)00004-6

Porcelli, D., and P. W. Swarzenski. 2003. The behavior of U- and Th-series nuclides in groundwater. Rev. Mineral. Geochemistry **52**. doi:10.2113/0520317

Rapaglia, J., E. Di Sipio, H. Bokuniewicz, G. M. Zuppi, L. Zaggia, A. Galgaro, and A. Beck. 2010. Groundwater connections under a barrier beach: A case study in the Venice Lagoon. Cont. Shelf Res. **30**: 119–126. doi:10.1016/j.csr.2009.10.001

Roberts, K. A., C. Xu, C.-C. Hung, M. H. Conte, and P. H. Santschi. 2009. Scavenging and fractionation of thorium vs. protactinium in the ocean, as determined from particle–water partitioning experiments with sediment trap material from the Gulf of Mexico and Sargasso Sea. Earth Planet. Sci. Lett. **286**: 131–138. doi:10.1016/J.EPSL.2009.06.029

Robinson, C. E., P. Xin, I. R. Santos, M. A. Charette, L. Li, and D. A. Barry. 2018. Groundwater dynamics in subterranean estuaries of coastal unconfined aquifers: Controls on submarine groundwater discharge and chemical inputs to the ocean. Adv. Water Resour. **115**: 315–331. doi:10.1016/J.ADVWATRES.2017.10.041

Robinson, C., L. Li, and H. Prommer. 2007. Tide-induced recirculation across the aquifer-ocean interface. Water Resour. Res. **43**. doi:10.1029/2006WR005679

Rodellas, V., J. Garcia-Orellana, G. Trezzi, P. Masque, T. C. Stieglitz, H. Bokuniewicz, J. K. Cochran, and E. Berdalet. 2017. Using the radium quartet to quantify submarine groundwater discharge and porewater exchange. Geochim. Cosmochim. Acta **196**: 58–73. doi:10.1016/j.gca.2016.09.016

Rodellas, V., T. C. Stieglitz, A. Andrisoa, P. G. Cook, P. Raimbault, J. J. Tamborski, P. van Beek, and O. Radakovitch. 2018. Groundwater-driven nutrient inputs to coastal lagoons: The relevance of lagoon water recirculation as a conveyor of dissolved nutrients. Sci. Total Environ. **642**. doi:10.1016/j.scitotenv.2018.06.095

Sadat-Noori, M., D. T. Maher, and I. R. Santos. 2016. Groundwater Discharge as a Source of Dissolved Carbon and Greenhouse Gases in a Subtropical Estuary. Estuaries and Coasts **39**: 639–656. doi:10.1007/s12237-015-0042-4

Santos, I. R., W. C. Burnett, T. Dittmar, I. G. N. A. Suryaputra, and J. Chanton. 2009. Tidal pumping drives nutrient and dissolved organic matter dynamics in a Gulf of Mexico subterranean estuary. Geochim. Cosmochim. Acta **73**: 1325–1339. doi:10.1016/J.GCA.2008.11.029

Santos, I. R., D. V Erler, D. R. Tait, and B. D. Eyre. 2010. Breathing of a coral cay: Tracing tidally driven seawater recirculation in permeable coral reef sediments. J. Geophys. Res. **115**: C12010. doi:10.1029/2010JC006510

Santos, I. R., B. D. Eyre, and M. Huettel. 2012. The driving forces of porewater and groundwater flow in permeable coastal sediments: A review. Estuar. Coast. Shelf Sci. **98**: 1–15. doi:10.1016/j.ecss.2011.10.024

Schopka, H. H., and L. A. Derry. 2012. Chemical weathering fluxes from volcanic islands and the importance of groundwater: the Hawaiian example. Earth Planet. Sci. Lett. **339**–**340**: 67–78. doi:10.1016/j.epsl.2012.05.028

Smith, C. G., J. E. Cable, J. B. Martin, and M. Roy. 2008. Evaluating the source and seasonality of submarine groundwater discharge using a radon-222 pore water transport model. Earth Planet. Sci. Lett. **273**: 312–322. doi:10.1016/j.epsl.2008.06.043

Sous, D., L. Petitjean, F. Bouchette, V. Rey, S. Meulé, F. Sabatier, and K. Martins. 2016. Field evidence of swash groundwater circulation in the microtidal rousty beach, France. Adv.

884 Water Resour. **97**: 144–155. doi:10.1016/J.ADVWATRES.2016.09.009

885 Stieglitz, T. C., P. van Beek, M. Souhaut, and P. G. Cook. 2013. Karstic groundwater discharge
886 and seawater recirculation through sediments in shallow coastal Mediterranean lagoons,
887 determined from water, salt and radon budgets. Mar. Chem. **156**: 73–84.

888 Sun, Y., and T. Torgersen. 1998a. The effects of water content and Mn-fiber surface conditions
889 on 224Ra measurement by 220Rn emanation. Mar. Chem. **62**: 299–306. doi:10.1016/S0304-
890 4203(98)00019-X

891 Sun, Y., and T. Torgersen. 1998b. Rapid and precise measurement method for adsorbed 224Ra
892 on sediments. Mar. Chem. **61**: 163–171.

893 Tamborski, J., S. Bejannin, J. Garcia-Orellana, and others. 2018. A comparison between water
894 circulation and terrestrially-driven dissolved silica fluxes to the Mediterranean Sea traced
895 using radium isotopes. Geochim. Cosmochim. Acta **238**: 496–515.
896 doi:10.1016/J.GCA.2018.07.022

897 Tamborski, J. J., J. K. Cochran, and H. J. Bokuniewicz. 2017. Application of 224Ra and 222Rn
898 for evaluating seawater residence times in a tidal subterranean estuary. Mar. Chem. **189**: 32–
899 45. doi:10.1016/j.marchem.2016.12.006

900 Tricca, A., G. J. Wasserburg, D. Porcelli, and M. Baskaran. 2001. The transport of U- and Th-
901 series nuclides in a sandy unconfined aquifer. Geochim. Cosmochim. Acta **65**: 1187–1210.
902 doi:10.1016/S0016-7037(00)00617-7

903 Webster, I. T., G. J. Hancock, and A. S. Murray. 1995. Modelling the effect of salinity on radium
904 desorption from sediments. Geochim. Cosmochim. Acta **59**: 2469–2476. doi:10.1016/0016-
905 7037(95)00141-7

906 Windom, H. L., W. S. Moore, L. F. H. Niencheski, and R. A. Jahnke. 2006. Submarine
907 groundwater discharge: A large, previously unrecognized source of dissolved iron to the
908 South Atlantic Ocean. Mar. Chem. **102**: 252–266. doi:10.1016/J.MARCHEM.2006.06.016

909 Xin, P., C. Robinson, L. Li, D. A. Barry, and R. Bakhtyar. 2010. Effects of wave forcing on a
910 subterranean estuary. Water Resour. Res. **46**. doi:10.1029/2010WR009632

911 ## ACKNOWLEDGEMENTS

912 This study was funded by ANR-MED-SGD (ANR-15-CE01-0004; PI: Pieter van Beek). The
913 postdoctoral fellowship of Joseph Tamborski and the PhD thesis of Simon Bejannin are
914 supported by FEDER funded by Europe and Région Occitanie Pyrénées-Méditerranée (SELECT
915 project). Valentí Rodellas acknowledges financial support from the European Union's Horizon
916 2020 research and innovation programme under the Marie Skłodowska-Curie grant agreement No

748896. Thomas Stieglitz holds a chair at RAction of the French Agence National de Recherche ANR (ANR-14-ACHN-0007-01, project medLOC), and is supported by the Labex OT-Med (ANR-11-LABEX-0061) funded by the "Investissements d'Avenir" program through the AMIDEX project (ANR-11- IDEX-0001-02). We are grateful to Kattalin Fortuné-Sans and Camille Pfleger (Parc Naturel Régional de la Narbonnaise en Méditerranée), Philippe Dussoullez and Jules Fleury for help with the beach topography survey, and Alain Le Berre (Cerema) for the wave buoy data. We thank Marc Souhaut for technical support in the LEGOS laboratory and at the LAFARA underground laboratory. We thank two anonymous reviewers for their helpful comments on an earlier draft of this manuscript.

FIGURE LEGENDS

Figure 1. The study site of La Franqui, located between La Palme lagoon and the Mediterranean Sea (Southern France, inset a; black square). The shore-perpendicular transect (Transect 1) was sampled monthly from May to September 2017, and again in November 2017. Transect 2 was sampled during May 2017 only. Google Earth imagery from May 14th 2017 is located approximately at the position of the white star (inset b). Lagoon surface water elevation measurement location is depicted by a circle (inset b; data from Parc Naturel Régional de la Narbonnaise en Méditerranée).

Figure 2. Sediment counting efficiency of the RaDeCC system determined from a ^{224}Ra standard addition spike, where the counting efficiency is equal to the slope of the cpm vs. dpm linear regression (A). ^{224}Ra sediment activity as a function of sample load (B). Note that the error bars are generally smaller than the symbol size.

Figure 3. Precipitation, wind speed and wave height during 2017. Wind and wave direction are plotted by color. Wind speed data is from "Meteo France" and wave height data is from CEREMA. Sampling periods are indicated by vertical gray lines. The dominant winds in the region include wind from the NW (i.e. "Tramontane", ~315°, yellow color on the plot) and wind from the sea (E; ~90°, blue color on the plot).

Figure 4. Spatial distribution of shallow pore water salinity (50 cm depth; hollow circles) with respect to lagoon surface water (filled triangle) and Mediterranean Sea (filled square) endmembers. During May, a second transect (Transect 2) was sampled and is depicted by diamonds connected with a dashed-line; note T1 is offset during May for clarity. Note the y and x-axes differ between plots.

Figure 5. Spatial distribution of shallow (50 cm depth) pore water ^{223}Ra (filled diamonds) and $^{224}Ra_{ex}$ (hollow circles) with respect to lagoon surface water (triangle) and Mediterranean Sea (square) endmembers.

Figure 6. Spatial distribution of shallow pore water (50 cm depth; hollow circles) ^{222}Rn with respect to lagoon surface water (filled triangle) and Mediterranean Sea (filled square) endmembers. ^{222}Rn was only sampled during May, June and November. Note the x-axes differ between plots.

Figure 7. Vertical distribution of salinity, ^{223}Ra, $^{224}Ra_{ex}$, DSi and Ba in pore water samples collected closest to the Mediterranean Sea (top) and closest to the lagoon (bottom), arranged by sampling season.

Figure 8. Spatial distribution of shallow pore water (50 cm depth; circles) DOC, DIC, DSi and Ba with respect to lagoon surface water (filled triangle) and Mediterranean Sea (filled square)

endmembers. Note that November is not included and only a limited number of samples were analyzed for DOC in May, August and September.

Figure 9. Distribution of shallow pore water (≤ 50 cm) $^{224}Ra_{ex}/^{223}Ra$ activity ratios and corresponding results from the $^{224}Ra_{ex}/^{223}Ra$ one-dimensional horizontal reactive-transport model. MED SW = Mediterranean surface water endmember; LW = lagoon surface water endmember. Note that transect 2 is included in May, with samples depicted as diamonds and model results as gray lines (a); T1 is offset during May for clarity. The solid black line is the model run with the lagoon water set as the boundary condition (A_o). Dashed lines represent ± 15% model uncertainty. Model results do not extend farther than 40 m from the lagoon endmember.

Figure 10. Vertical distribution of ^{222}Rn, ^{223}Ra and $^{224}Ra_{ex}$ in pore water samples collected closest to the Mediterranean Sea. The thick dashed-line is the one-dimensional vertical reactive transport model result for June (^{222}Rn v = 30 cm d^{-1}; ^{223}Ra v = 14 cm d^{-1}; ^{224}Ra v = 14 cm d^{-1}) and the thin dashed-line is the vertical model result for November (^{222}Rn v = 90 cm d^{-1}; ^{223}Ra v = 52 cm d^{-1}; ^{224}Ra v = 35 cm d^{-1}).

TABLES

Table 1. Bulk solid-phase radionuclide activities and measured distribution coefficients (K_D) for a salinity of 27 and 38.

ID	Distance from sea	^{226}Ra	^{228}Ra	^{228}Th	^{228}Th/^{226}Ra	K_D (S = 27)	K_D (S = 38)
	m	*dpm g^{-1}*	*dpm g^{-1}*	*dpm g^{-1}*		*cm^3 g^{-1}*	*cm^3 g^{-1}*
5-PW3-A	23	0.57 ± 0.02	0.66 ± 0.04	0.67 ± 0.01	1.17 ± 0.04	-	-
5-2-PW3-A	44	0.58 ± 0.04	0.41 ± 0.07	0.79 ± 0.07	1.37 ± 0.15	3.1	2.1
5-PW5-A	43	0.58 ± 0.02	0.47 ± 0.03	0.61 ± 0.02	1.05 ± 0.05	2.4	1.4
5-PW7-A	63	0.50 ± 0.02	0.55 ± 0.04	0.56 ± 0.01	1.12 ± 0.05	-	-

995 **Table 2.** Sediment surface-exchangeable ^{223}Ra and ^{224}Ra activities, determined via RaDeCC.

ID	Distance from sea	^{223}Ra	^{224}Ra	^{224}Ra/^{223}Ra
	m	*dpm g^{-1}*	*dpm g^{-1}*	
5-PW3-A	23	0.0022 ± 0.0003	0.034 ± 0.001	15.7
5-PW5-A	43	0.0025 ± 0.0005	0.038 ± 0.002	15.2
5-PW6-A	53	0.0024 ± 0.0005	0.050 ± 0.002	20.9
5-PW7-A	63	0.0028 ± 0.0003	0.041 ± 0.001	15.0
AVG ± STD		***0.0025 ± 0.002***	***0.041 ± 0.006***	***16.7 ± 2.4***

996

997

998

999

1000

1001

1002

1003

1004

1005

1006

1007

1008

Table 3. Sediment equilibration results. Total $^{224}Ra/^{222}Rn$ activity ratios consider a mean surface-exchangeable ^{224}Ra activity of 0.041 ± 0.006 dpm g^{-1} (176 ± 25 dpm L^{-1}).

	^{222}Rn*	^{223}Ra	^{224}Ra	$^{224}Ra/^{222}Rn$	$^{224}Ra/^{222}Rn$
	dpm L^{-1}	*dpm L^{-1}*	*dpm L^{-1}*	*dissolved*	*total*
Salinity 27	160 ± 20	2.5 ± 0.3	29.0 ± 3.0	0.18 ± 0.03	1.28 ± 0.22
Salinity 38	160 ± 20	3.0 ± 0.2	52.5 ± 4.0	0.33 ± 0.05	1.43 ± 0.24

*^{222}Rn equilibration results are only for a salinity of 38 but assumed to be representative for all salinities (minor influence of water salinity on ^{222}Rn partitioning).

Table 4. Lagoon surface water elevation and water table elevation above sea level. Water table elevation measurements are taken closest to the lagoon edge, approximately 73 m from the Mediterranean Sea and are corrected for the elevation of the beach surface (measured during June). November is not included. Lagoon surface water elevation data is from the Parc Naturel Régional de la Narbonnaise en Méditerranée monitoring station Coussoules (Fig. 1).

	Surface Water Elevation	Water Table Elevation
	m	*m*
May	0.85	0.36
June	0.75	0.29
July	0.60	0.24
August	0.53	0.19
September	0.45	0.13
November	0.55	-

Table 5. Parameters used in the one-dimensional reactive-transport model. Note that the term K is only interpolated for the horizontal model. The vertical model uses the term $[P/(1+K)]$ determined from sediment equilibration experiments for seawater salinity. The radionuclide activity of the Mediterranean Sea and lagoon surface endmember is taken as the value measured for each respective sampling campaign.

Term	Definition	Value	Uncertainty	Units
φ	Porosity	0.38	0.01	-
ρ	Sediment Density	2.65	-	g cm^{-3}
P_{222}	^{222}Rn Production	160	20	dpm L^{-1}
P_{223}	^{223}Ra Production	10.6	1.0	dpm L^{-1}
P_{224}	^{224}Ra Production	176	25	dpm L^{-1}
K	Ra Partition Coefficient	linear interpolation from salinity distribution*	-	-
Δx	Change in distance	measured from boundary condition		m
λ_{222}	^{222}Rn Decay Constant	0.181	-	d^{-1}
λ_{223}	^{223}Ra Decay Constant	0.061	-	d^{-1}
λ_{224}	^{224}Ra Decay Constant	0.193	-	d^{-1}
A_{sea}^{222}	^{222}Rn coastal Mediterranean Sea	4 - 9	20-40%	dpm L^{-1}
A_{sea}^{223}	^{223}Ra coastal Mediterranean Sea	0.1 - 0.3	7-9%	dpm L^{-1}
A_{sea}^{224}	^{224}Ra coastal Mediterranean Sea	3.4 - 8.3	5-9%	dpm L^{-1}
A_{lagoon}^{223}	^{223}Ra Lagoon Surface Water	0.1 - 1.3	7 - 14%	dpm L^{-1}
A_{lagoon}^{224}	^{224}Ra Lagoon Surface Water	3.1 - 26	6 - 14%	dpm L^{-1}
v	1-D advection velocity	modeled from curve-fitting	15%	m d^{-1}

*K is linearly interpolated between values of 1.5 – 2.9 for salinities of 27 – 38.

Table 6. Summary of Fisher's F test (Pr>F, df = 3) multiple linear regression model results for seawater circulation through the swash-zone, with corresponding regression coefficients (R^2). Seawater circulation advective velocities (dependent variable) are determined from the ^{223}Ra reactive-transport model. Wind speed and wind direction are the variables used in the "Wind" regression; wind-setup and wave-runup are the variables used in the "Waves" regression. Statistically significant model results are indicated in bold.

Time (h)	Wind - R^2	Wind - Pr>F	Waves - R^2	Waves - Pr>F
6	0.78	0.10	**0.87**	**0.05**
12	0.79	0.10	0.75	0.12
24	0.64	0.21	0.67	0.19
48	**0.92**	**0.02**	0.09	0.86
72	**0.87**	**0.05**	0.20	0.86
168	0.20	0.71	0.38	0.49
336	0.20	0.71	0.24	0.66

Table 7. Summary of water exchange, DSi (mmol m^{-1} d^{-1}), DIC (mmol m^{-1} d^{-1}) and Ba (µmol m^{-1} d^{-1}) fluxes, arranged by sampling season. Lagoon-sea water exchange is only considered for May, June and July. Swash-zone seawater circulation flushing rates are derived from ^{223}Ra profiles; Ba fluxes are not estimated for seawater circulation.

Date	Flushing Rate		Concentration	Si Flux mmol m^{-1} d^{-1}	Concentration	C Flux mmol m^{-1} d^{-1}	Concentration	Ba Flux µmol m^{-1} d^{-1}
	cm d^{-1}	m^3 d^{-1} m^{-1}	µM Si		µM C		nM Ba	
*Horizontal Transport (lagoon)**								
9-May	85	0.3	31	10	3,280	1,100	220	70
22-Jun	30	0.1	35	4	3,610	410	120	10
6-Jul	20	0.1	44	3	4,260	320	150	10
*Seawater Circulation^*								
9-May	30	1.1	4	5	25	29	-	-
22-Jun	14	0.5	11	6	27	14	-	-
6-Jul	10	0.4	9	3	53	20	-	-
30-Aug	25	1.0	9	8	52	50	-	-
25-Sep	55	2.1	-	-	-	-	-	-
17-Nov	52	2.0	4	7	110	220	-	-

*Exchange zone depth = 1 m; DSi, DIC and Ba concentrations taken at ~x=20 m from the sea.

^Swash-zone width = 10 m; DSi and DIC concentrations are net enrichments over coastal Mediterranean Sea surface endmembers.

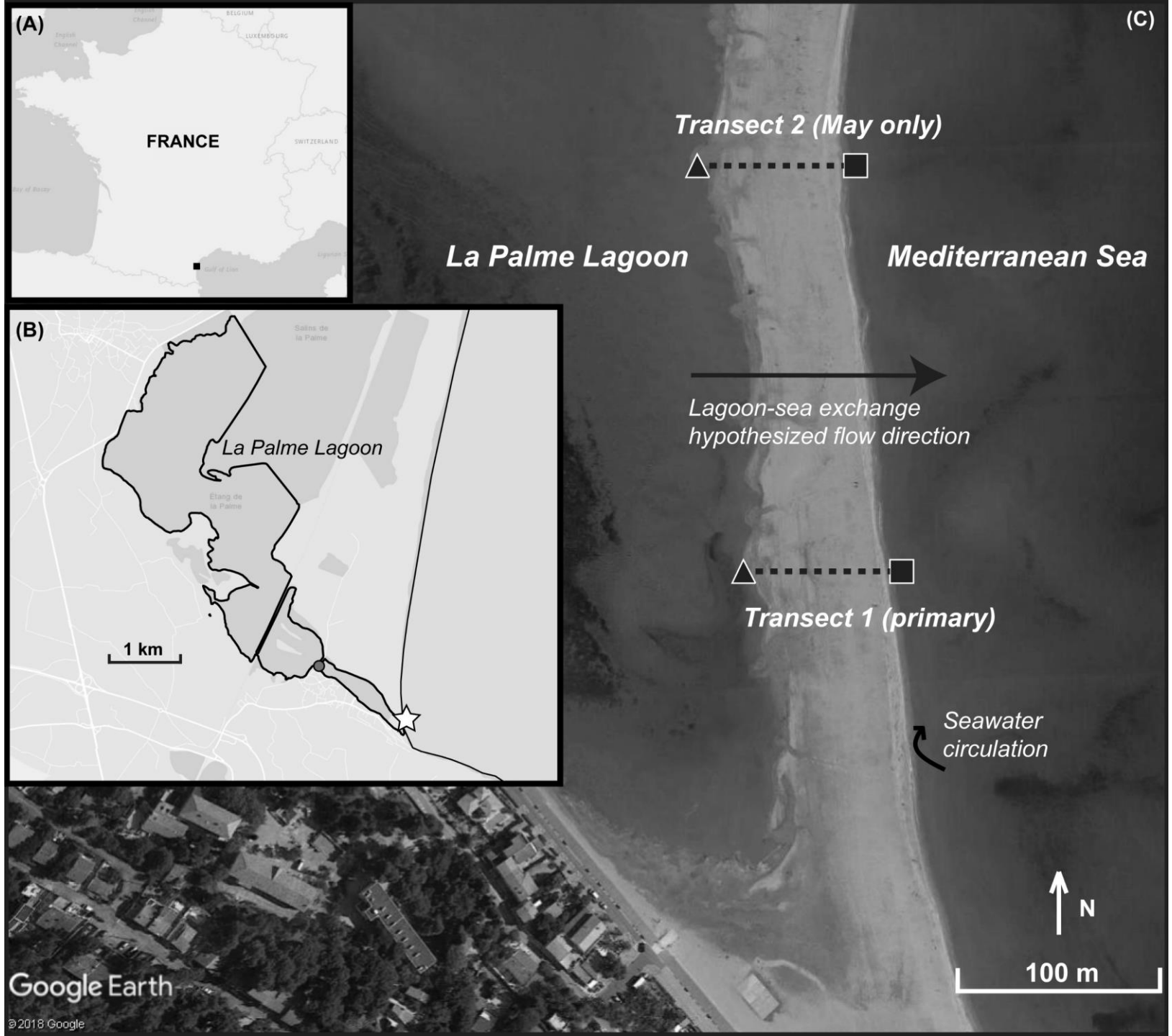
(A)
BELGIUM
LUXEMBOURG
FRANCE
SWITZERLAND
(B)
Salins de la Palme
La Palme Lagoon
Etang de la Palme
1 km
(C)
Transect 2 (May only)
La Palme Lagoon
Mediterranean Sea
Lagoon-sea exchange hypothesized flow direction
Transect 1 (primary)
Seawater circulation
N
100 m
Google Earth
©2018 Google

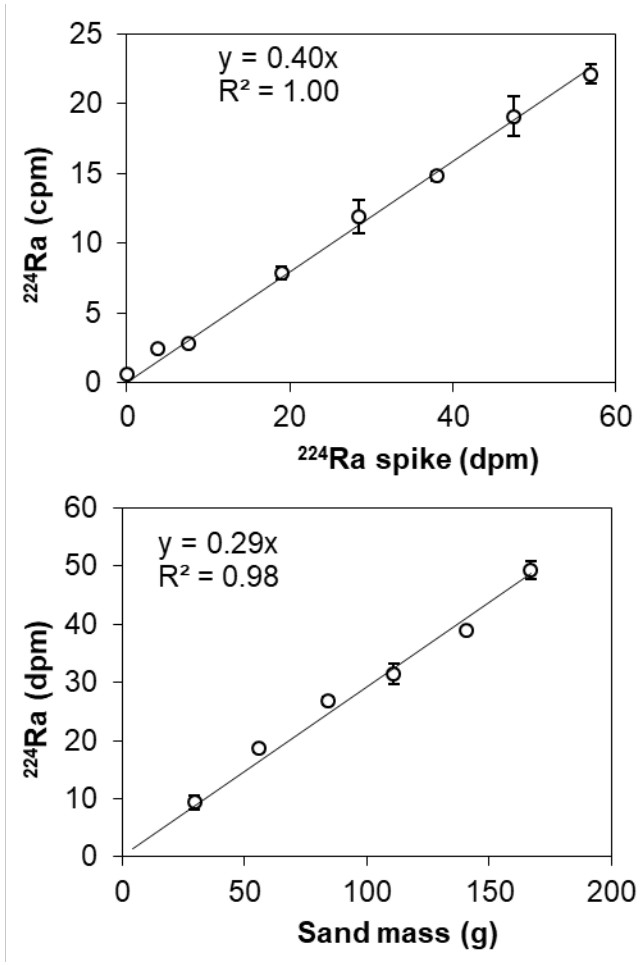
y = 0.40x
R² = 1.00
224Ra (cpm)
224Ra spike (dpm)
0
5
10
15
20
25
0
20
40
60
y = 0.29x
R² = 0.98
224Ra (dpm)
Sand mass (g)
0
10
20
30
40
50
60
0
50
100
150
200

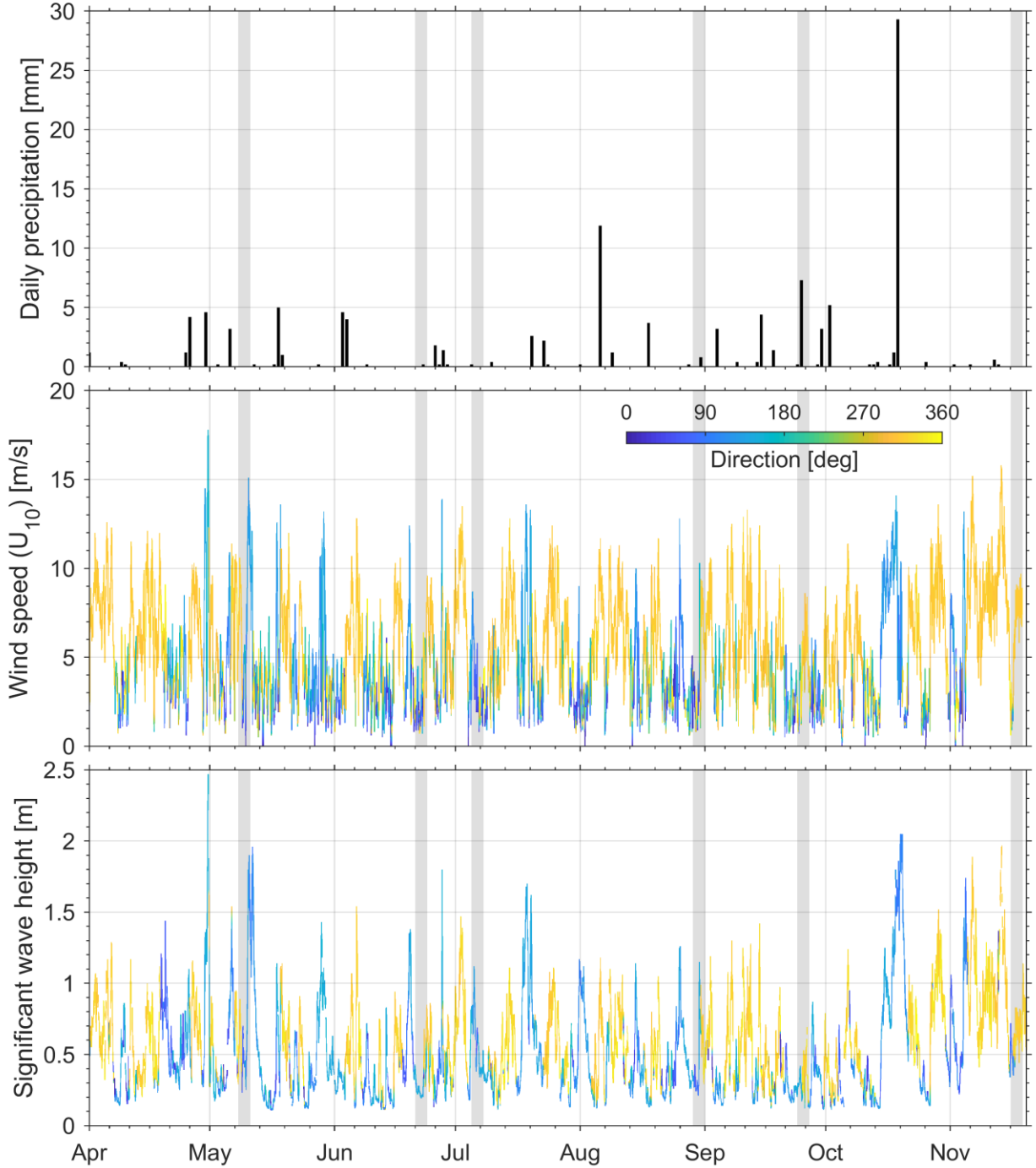
Daily precipitation [mm]
30
25
20
15
10
5
0
Wind speed (U_{10}) [m/s]
20
15
10
5
0
0
90
180
270
360
Direction [deg]
Significant wave height [m]
2.5
2
1.5
1
0.5
0
Apr
May
Jun
Jul
Aug
Sep
Oct
Nov

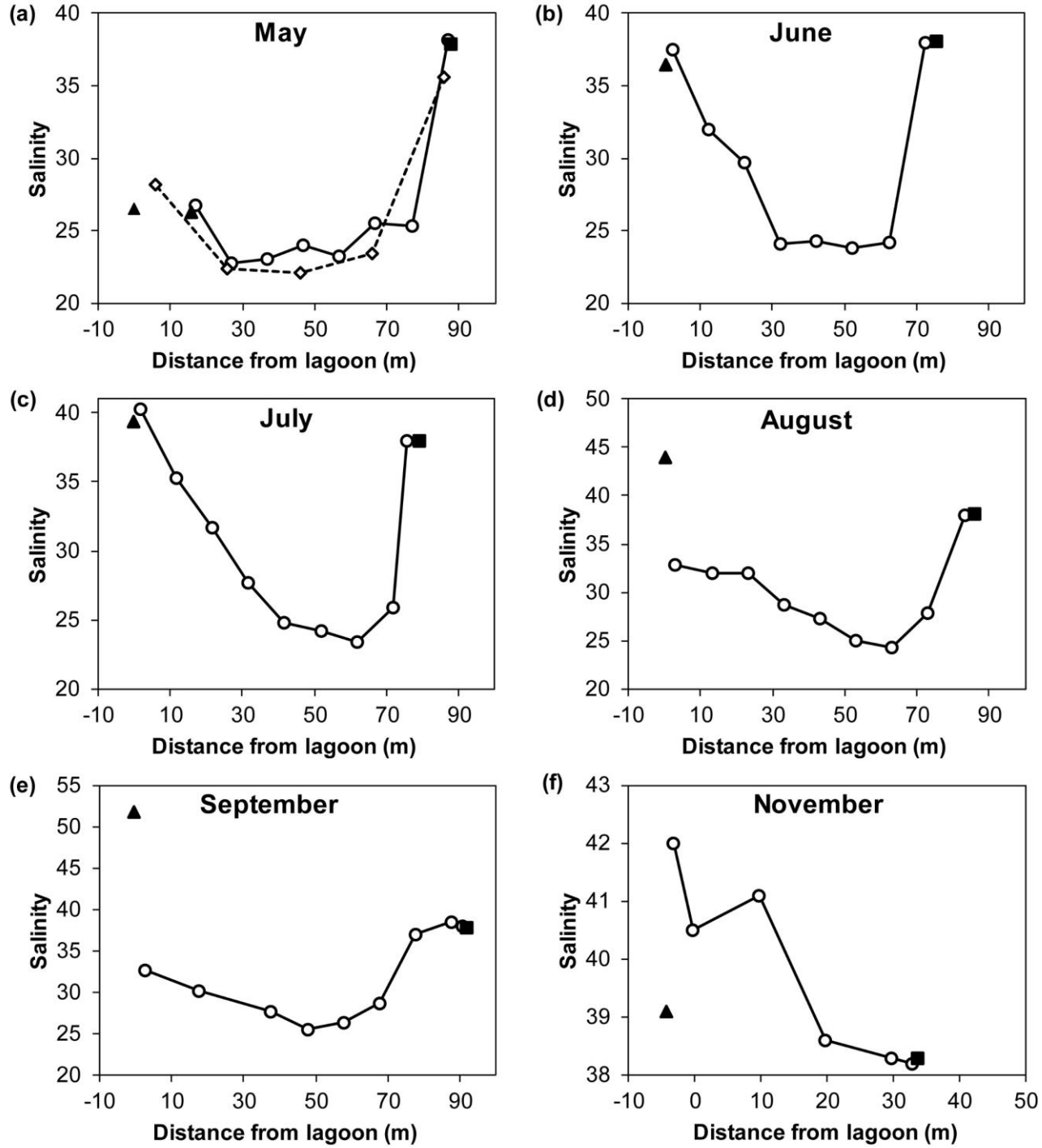
(a)
May
Salinity
Distance from lagoon (m)
(b)
June
Salinity
Distance from lagoon (m)
(c)
July
Salinity
Distance from lagoon (m)
(d)
August
Salinity
Distance from lagoon (m)
(e)
September
Salinity
Distance from lagoon (m)
(f)
November
Salinity
Distance from lagoon (m)

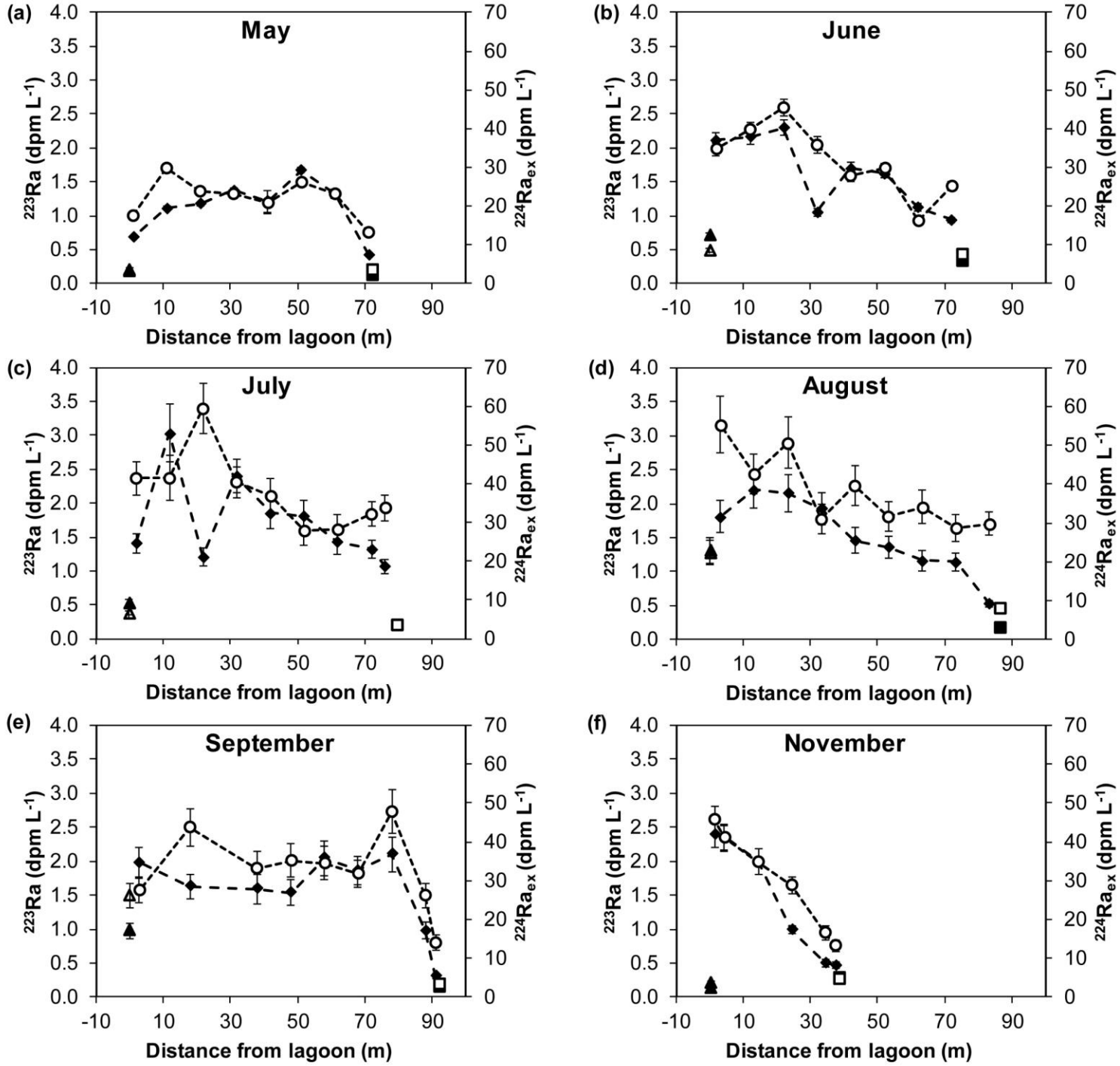
(a)
May
(b)
June
(c)
July
(d)
August
(e)
September
(f)
November
^{223}Ra (dpm L^{-1})
^{224}Ra$_{ex}$ (dpm L^{-1})
Distance from lagoon (m)

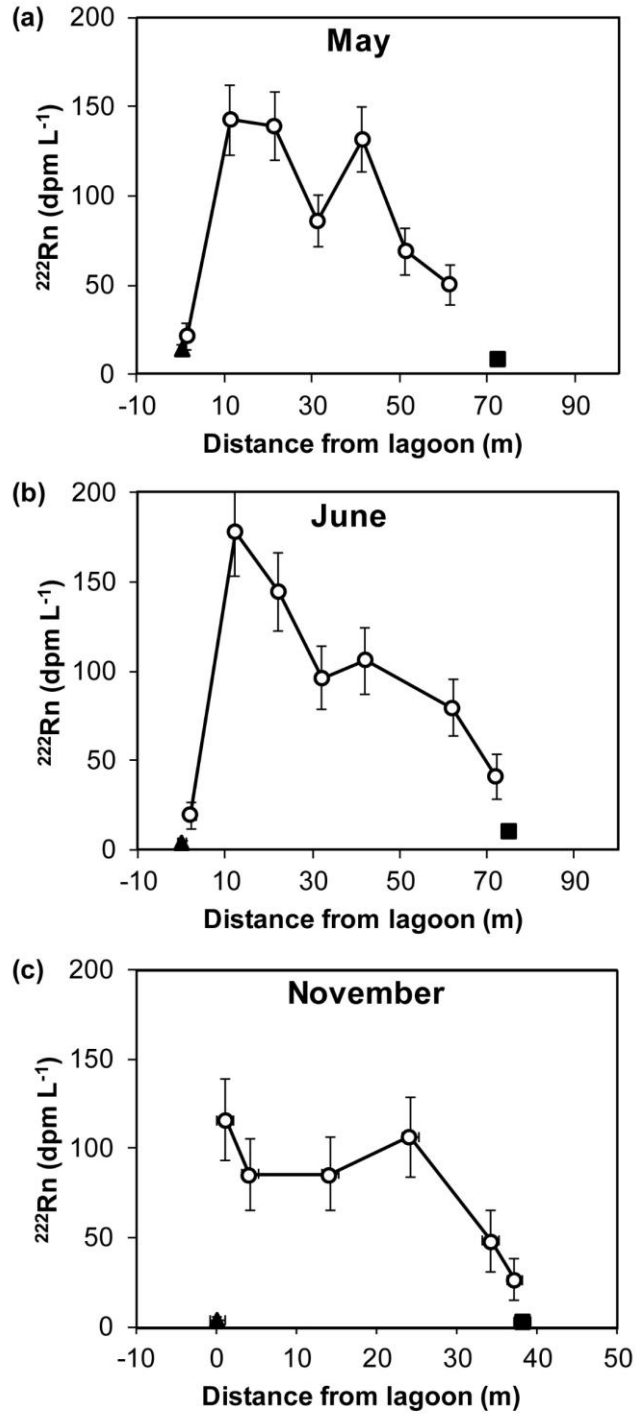
(a)
May
^{222}Rn (dpm L^{-1})
Distance from lagoon (m)
(b)
June
^{222}Rn (dpm L^{-1})
Distance from lagoon (m)
(c)
November
^{222}Rn (dpm L^{-1})
Distance from lagoon (m)

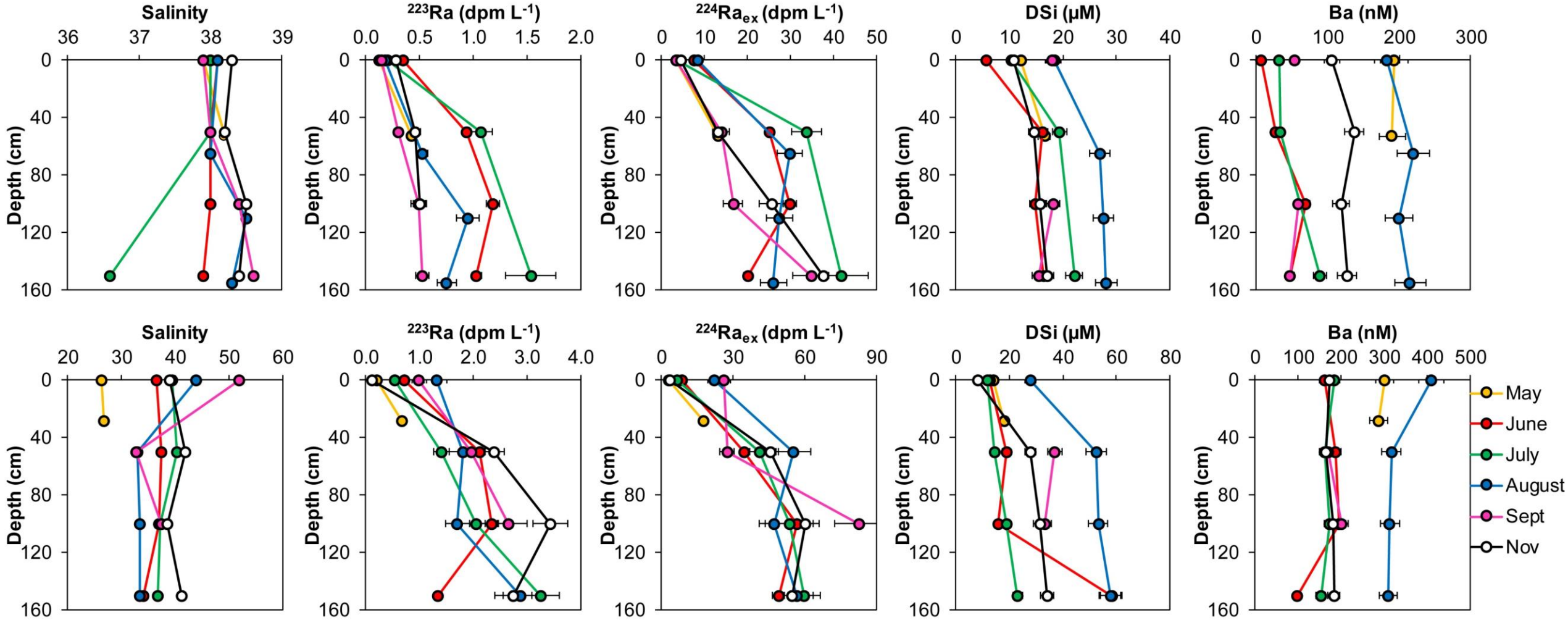
Salinity
36
37
38
39
^{223}Ra (dpm L^{-1})
0.0
0.5
1.0
1.5
2.0
^{224}Ra$_{ex}$ (dpm L^{-1})
0
10
20
30
40
50
DSi (μM)
0
10
20
30
40
Ba (nM)
0
100
200
300
Depth (cm)
0
40
80
120
160
Salinity
20
30
40
50
60
^{223}Ra (dpm L^{-1})
0.0
1.0
2.0
3.0
4.0
^{224}Ra$_{ex}$ (dpm L^{-1})
0
30
60
90
DSi (μM)
0
20
40
60
80
Ba (nM)
0
100
200
300
400
500
Depth (cm)
May
June
July
August
Sept
Nov

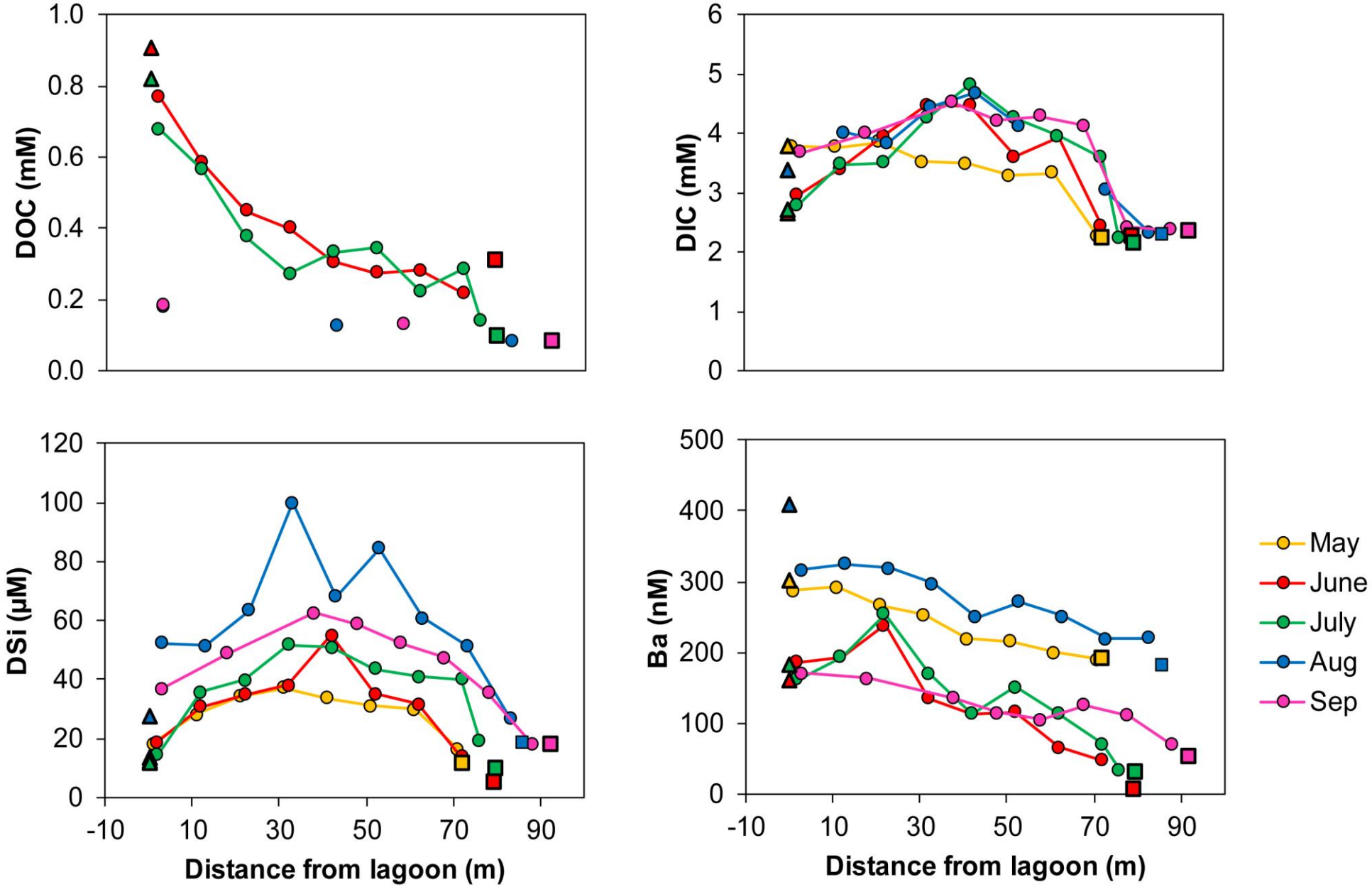
DOC (mM)
1.0
0.8
0.6
0.4
0.2
0.0
DIC (mM)
6
5
4
3
2
1
0
DSi (µM)
120
100
80
60
40
20
0
-10
10
30
50
70
90
Distance from lagoon (m)
Ba (nM)
500
400
300
200
100
0
-10
10
30
50
70
90
Distance from lagoon (m)
May
June
July
Aug
Sep

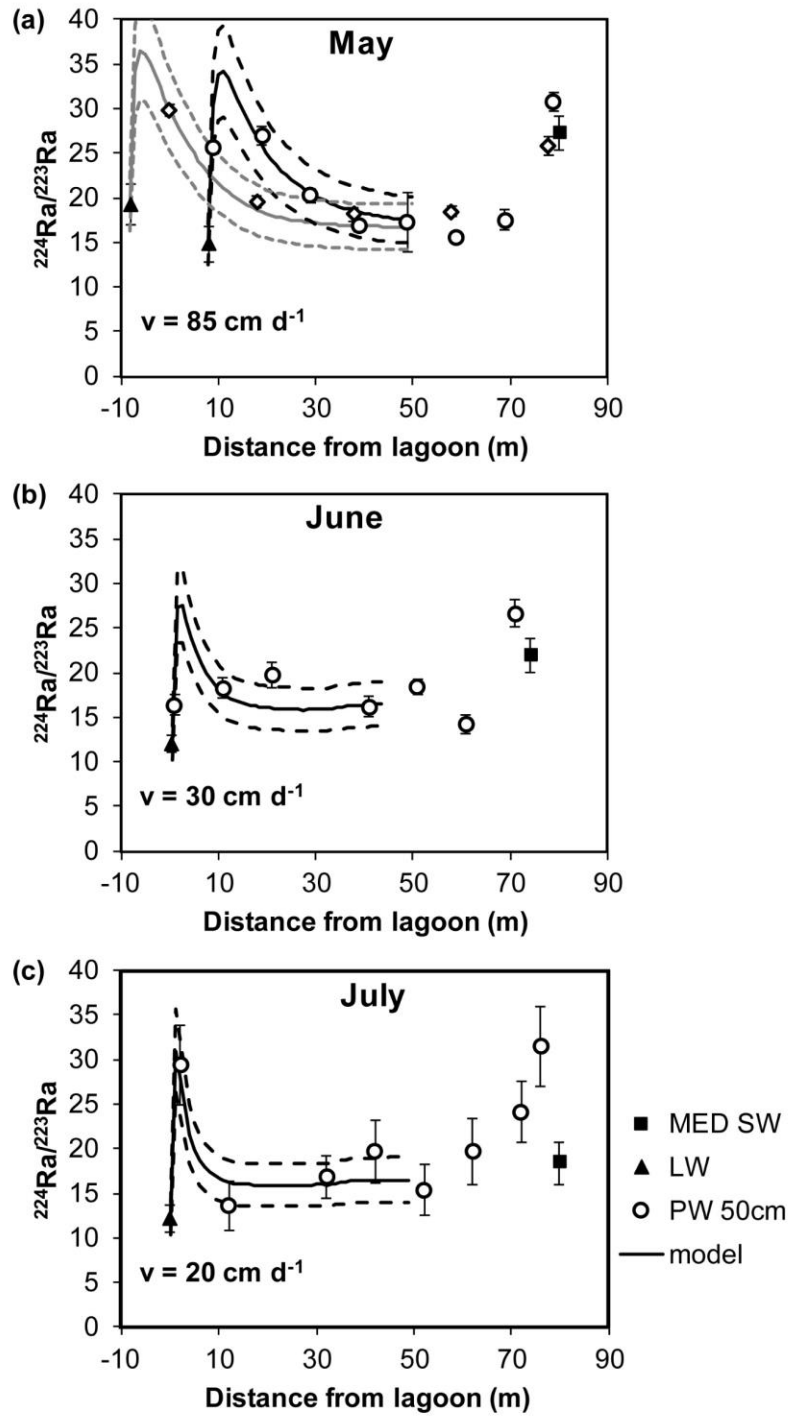
(a)
May
$^{224}Ra/^{223}Ra$
v = 85 cm d^{-1}
Distance from lagoon (m)
(b)
June
$^{224}Ra/^{223}Ra$
v = 30 cm d^{-1}
Distance from lagoon (m)
(c)
July
$^{224}Ra/^{223}Ra$
v = 20 cm d^{-1}
Distance from lagoon (m)
MED SW
LW
PW 50cm
model

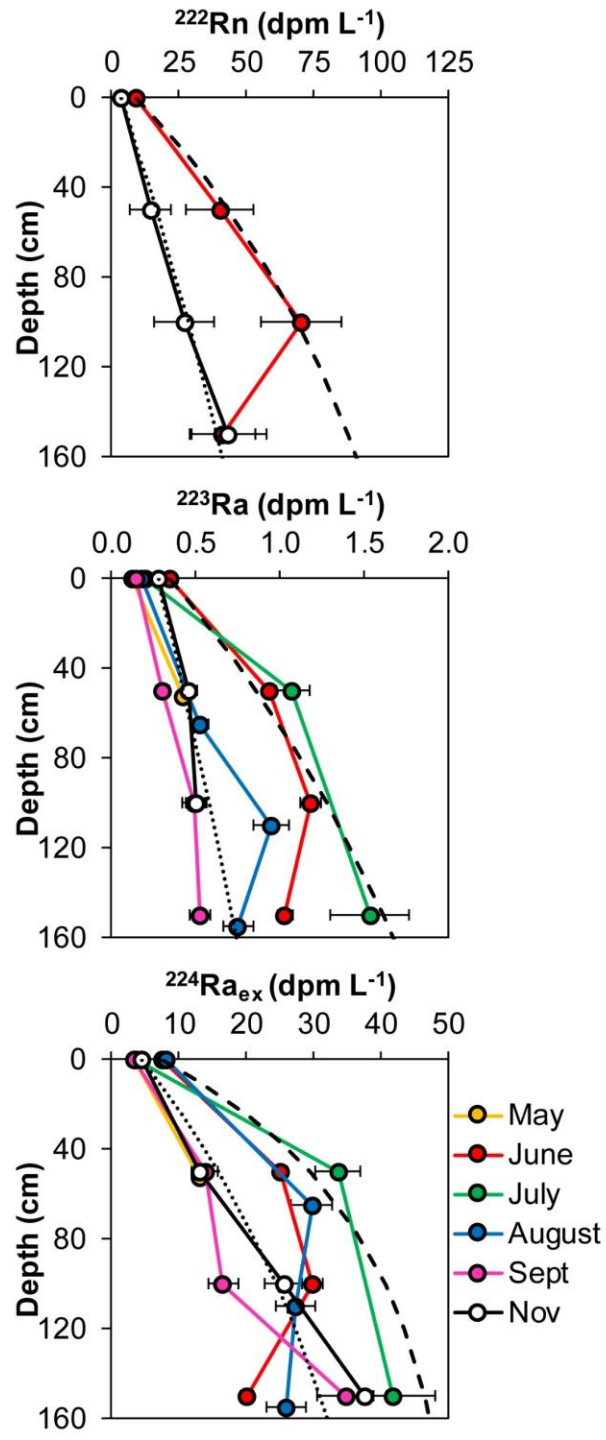
^{222}Rn (dpm L^{-1})
0 25 50 75 100 125
^{223}Ra (dpm L^{-1})
0.0 0.5 1.0 1.5 2.0
^{224}Ra$_{ex}$ (dpm L^{-1})
0 10 20 30 40 50
Depth (cm)
0 40 80 120 160
May
June
July
August
Sept
Nov